

General relativistic radiation hydrodynamics of accretion flows – I. Bondi–Hoyle accretion

O. Zanotti,^{1*} C. Roedig,¹ L. Rezzolla^{1,2} and L. Del Zanna³

¹Max-Planck-Institut für Gravitationsphysik, Albert Einstein Institut, Am Mühlenberg 1, 14476 Golm, Germany

²Department of Physics, Louisiana State University, Baton Rouge, LA 70803, USA

³Dipartimento di Fisica e Astronomia, Università di Firenze, Largo E. Fermi 2, 50125 Firenze, Italy

Accepted 2011 July 14. Received 2011 July 14; in original form 2011 May 27

ABSTRACT

We present a new code for performing general-relativistic radiation-hydrodynamic simulations of accretion flows on to black holes. The radiation field is treated in the optically thick approximation, with the opacity contributed by the Thomson scattering and thermal bremsstrahlung. Our analysis concentrates on a detailed numerical investigation of hot ($T \sim 10^{10}$ K) two-dimensional, Bondi–Hoyle accretion flows with various Mach numbers. The asymptotic velocity is in the range $v_\infty \sim (0.08\text{--}0.18)c$, while the initial rest-mass density is of the order of a few $\rho \sim 10^{-12}$ g cm⁻³. We find significant differences with respect to purely hydrodynamical evolutions. In particular, once the system relaxes to a radiation-pressure-dominated regime, the accretion rates become about two orders of magnitude smaller than in the purely hydrodynamical case, remaining however super-Eddington as well as the luminosities. Furthermore, when increasing the Mach number of the inflowing gas, the accretion rates become smaller because of the smaller cross-section of the black hole, but the luminosities increase as a result of a stronger emission in the shocked regions. Overall, our approach provides the first self-consistent calculation of the Bondi–Hoyle luminosity, most of which is emitted within $r \sim 100M$ from the black hole, with typical values $L/L_{\text{Edd}} \simeq 1\text{--}7$, and corresponding energy efficiencies $\eta_{\text{B\&H}} \sim 0.09\text{--}0.5$. The possibility of computing luminosities self-consistently has also allowed us to compare with the bremsstrahlung luminosity often used in modelling the electromagnetic counterparts to supermassive black hole binaries, to find that in the optically thick regime these more crude estimates are about 20 times larger than our radiation-hydrodynamic results.

Key words: accretion, accretion discs – black hole physics – radiation mechanisms: general – relativistic processes.

1 INTRODUCTION

Numerical relativity faces an embarrassing gap between the accuracy with which it computes the gravitational-wave emission from the dynamics of compact objects such as black holes and neutron stars (Duez 2010; McWilliams 2011; Rezzolla et al. 2011; Sekiguchi et al. 2011) and the very rough estimates of the electromagnetic emission that can be currently computed with state-of-the-art numerical codes (Farris et al. 2008; Palenzuela et al. 2009; Mösta et al. 2010; Bode et al. 2010; Zanotti et al. 2010). The strongest limitation preventing a more realistic description of the emitted electromagnetic radiation is the modelling of radiative transfer in the gas, which is often neglected in relativistic calculations in view of the large computational costs involved. This problem is of course common to a large class of relativistic simulations, but it becomes

particularly apparent in those cases where an accurate computation of the emitted luminosity is at least as important as providing a faithful description of the dynamics. Among such cases, accretion on to compact objects is perhaps the most important one.

Until a few years ago, the time-dependent solution of the relativistic radiation-hydrodynamic equations of accretion flows was performed in one spatial dimension only and, typically, through Lagrangian finite-difference schemes or through the so-called linearized block-implicit algorithms. Starting from the pioneering works by Gilden & Wheeler (1980) and Vitello (1984), relevant results concerning spherical accretion on to black holes were obtained with a Lagrangian code by Zampieri, Miller & Turolla (1996), who were able to solve the radiation-hydrodynamic equations both in the optically thin and in the optically thick regime, by means of the projected symmetric trace-free (PSTF) moment formalism introduced by Thorne (1981) and subsequently reformulated by Rezzolla & Miller (1994) for spherical flows. Such formalism provides one of the most accurate approximations to the solution of the radiation

*E-mail: zanotti@aei.mpg.de

transfer equations, and, in analogy to what is done in fluid dynamics, it allows us to define moments of the radiation field similarly to how density, momentum and pressure of a medium are defined as moments of the distribution function. As a result, instead of following rays, the moment equations are solved directly with an Eulerian or a Lagrangian code.¹

Despite these initial efforts, the time-dependent solution of the relativistic radiation-hydrodynamic equations in more than one spatial dimensions remains very challenging. Nowadays, the multi-dimensional numerical codes available can be divided into two major classes, accounting for, separately, the optically thin regime or the optically thick one. The former class is mainly focused on providing a realistic modelling of core-collapse supernovae, by employing Boltzmann neutrino transport, state-of-the-art neutrino interactions, and general relativity. Relevant achievements have been obtained over the years by Herant et al. (1994), Janka & Mueller (1995, 1996), Mezzacappa et al. (2001), Bruenn, Nisco & Mezzacappa (2001), Liebendörfer et al. (2001, 2005), Messer et al. (2008), Müller, Janka & Dimmelmeier (2010), who, among other things, showed the importance of multi-dimensional simulations to model the shock revival via neutrinos in a supernova explosion. In a different physical context, namely that of accretion discs around black holes, but still in the optically thin regime, Noble, Krolik & Hawley (2009) considered an approximate treatment in which radiation is described through a loss term in the energy equation. They used fully relativistic ray-tracing techniques to compute the luminosity received by distant observers. For a disc with aspect ratio $H/r \simeq 0.1$ accreting on to a black hole with spin parameter $a = 0.9$, they found a significant dissipation beyond that predicted by the classical model by Novikov & Thorne (1973).

The numerical investigation of the optically thick regime, on the other hand, has received less attention. The seminal work by Hsieh & Spiegel (1976) already set the basis for the formulation of the relativistic radiation-hydrodynamic equations in conservation form and therefore suitable for an Eulerian numerical implementation. Later on, interesting advances were obtained by Shapiro (1996), Park (2006) and Takahashi (2007). Finally, Farris et al. (2008) have shown that for optically thick gases and grey-body opacities, the general-relativistic radiation-hydrodynamic equations can indeed be written in conservation form, thus allowing for the use of numerical methods based on Riemann solvers that have been successfully adopted by many relativistic hydrodynamics and magnetohydrodynamic codes. Very recently, and while this paper was being completed, Shibata et al. (2011) have presented a modified truncated moment formalism allowing for the conservative formulation of the relativistic radiation-hydrodynamic equations both in the optically thin and in the optically thick limit. This formulation could represent a major step forward with respect to present leakage schemes accounting for the free streaming of radiation (Sekiguchi 2010; Sekiguchi et al. 2011).

In this paper, which is the first of a series, we extend our ECHO code (Del Zanna et al. 2007) by following the strategy suggested by Farris et al. (2008), and concentrate on one of the simplest accretion flow scenarios, namely the Bondi–Hoyle accretion on to a

black hole. This problem has recently been studied by Farris, Liu & Shapiro (2010) in the context of merging supermassive black hole binaries in full general relativity, but neglecting the back-reaction of radiation on to matter. By assuming that opacity is contributed by the Thomson scattering and thermal bremsstrahlung, we compute here the luminosity emitted in hot Bondi–Hoyle accretion on to a black hole. As the flow relaxes to a radiation-pressure-dominated regime, we find significant differences with respect to purely hydrodynamical evolutions. In particular, the accretion rates drop off by about two orders of magnitude when compared to the purely hydrodynamical case, remaining however super-Eddington. Furthermore, we find that larger inflow velocities lead to smaller accretion rates (because of the smaller cross-section of the black hole) but to larger luminosities (because of the stronger emission in the shocked regions).

The plan of the paper is as follows. We first describe the numerical methods in Section 2 while the validation of the code is presented in Section 3. Section 4, on the other hand, is devoted to radiative Bondi–Hoyle accretion flows and contains the main results of our work. The conclusions are presented in Section 5. We assume a signature $(-, +, +, +)$ for the space–time metric and we will use Greek letters (running from 0 to 3) for four-dimensional space–time tensor components, while Latin letters (running from 1 to 3) will be employed for three-dimensional spatial tensor components. Moreover, we set $c = 1$, $G = 10^{-10}$ and extend the geometric units by setting $m_p/k_B = 1$, where m_p is the mass of the proton, while k_B is the Boltzmann constant. We have maintained c , G and k_B in an explicit form in those expressions of particular physical interest. Appendix A describes the extended geometrized system of units adopted in the code.

2 RELATIVISTIC RADIATION HYDRODYNAMICS

2.1 Covariant formulation

The total momentum-energy tensor $T^{\alpha\beta}$ of a fluid immersed in a radiation field comprises two terms: $T^{\alpha\beta} = T_m^{\alpha\beta} + T_r^{\alpha\beta}$. The first one is the ordinary one describing the energy and momentum of the matter

$$T_m^{\alpha\beta} = \rho h u^\alpha u^\beta + p g^{\alpha\beta}, \quad (1)$$

where $g^{\alpha\beta}$ is the space–time metric tensor, u^α is the four-velocity of the fluid, while ρ , $h = 1 + \epsilon + p/\rho$, ϵ and p are the rest-mass density, the specific enthalpy, the specific internal energy and the thermal pressure, respectively. All of these quantities are measured in the comoving frame of the fluid. The thermal pressure is related to ρ and ϵ through an equation of state (EOS), and we will here consider an ideal gas, for which the EOS is expressed as

$$p = \rho\epsilon(\gamma - 1), \quad (2)$$

where γ is the (constant) adiabatic index of the gas. The second term describes instead the radiation field and is given by (Mihalas & Mihalas 1999; Shapiro 1996)

$$T_r^{\alpha\beta} = \frac{1}{c} \int I_\nu N^\alpha N^\beta d\nu d\Omega, \quad (3)$$

where $I_\nu = I_\nu(x^\alpha, N^i, \nu)$ is the specific intensity² of the radiation, N^α is the four-vector defining the photon propagation direction, $d\nu$

¹ In a non-relativistic context, recent interesting developments have been reported by Petkova & Springel (2009, 2010), who adopted the moment formalism within the smoothed particle hydrodynamics (SPH) GADGET code and used a variable Eddington tensor as a closure relation, following the Optically Thin Variable Eddington Tensor suggestion of Gnedin & Abel (2001).

² We note that I_ν is an energy flux per unit time, frequency and solid angle, so that in cgs units it has dimensions of $\text{erg cm}^{-2} \text{s}^{-1} \text{Hz}^{-1} \text{sr}^{-1}$.

is the infinitesimal frequency and $d\Omega$ is the infinitesimal solid angle around the direction of propagation. We recall that the direction of propagation of the photon is defined as $N^\alpha \equiv p^\alpha/h_{\text{pl}}v$, where p^α is the photon four-momentum, while h_{pl} and v are, respectively, the Planck constant and the photon frequency as measured in the comoving frame of the fluid. Since the two terms $v dv d\Omega$ and I_ν/v^3 are relativistic invariants (Rybicki & Lightman 1986), their product with the tensor $p^\alpha p^\beta$ is still a tensor, and indeed it provides the integrand of equation (3).

In the frame comoving with the fluid, the moments of the radiation field are the energy density, the radiation flux and the radiation stress tensor, which are respectively given by

$$E_r = \frac{1}{c} \int I_\nu dv d\Omega, \quad (4)$$

$$F_r^\alpha = h_{\text{pl}}^\alpha \int I_\nu dv d\Omega N^\beta, \quad (5)$$

$$P_r^{\alpha\beta} = \frac{1}{c} \int I_\nu dv d\Omega N^\alpha N^\beta, \quad (6)$$

where the tensor $h^{\alpha\beta} = g^{\alpha\beta} + u^\alpha u^\beta$ projects any other tensor into the space orthogonal to u^α , namely $h^{\alpha\beta} u_\alpha = 0$. In terms of such moments the radiation energy-momentum tensor $T_r^{\alpha\beta}$ can be rewritten as (Hsieh & Spiegel 1976)

$$T_r^{\alpha\beta} = (E_r + \mathcal{P}_r) u^\alpha u^\beta + F_r^\alpha u^\beta + u^\alpha F_r^\beta + \mathcal{P}_r g^{\alpha\beta}, \quad (7)$$

where E_r and \mathcal{P}_r are the radiation energy density and pressure, respectively. As in Farris et al. (2008), we make the additional and strong physical assumption that the radiation is very close to being isotropic in the comoving frame of the fluid, thus mimicking the conditions of the optically thick regime. However, while the radiation pressure is actually set to be $\mathcal{P}_r = E_r/3$, as the isotropic assumption implies, the radiation flux is allowed to assume non-vanishing values, although with the constraint that $F_r^i/E_r \ll 1$. Hence, the radiation field is only approximately isotropic.

The full set of equations describing the dynamics of the system is

$$\nabla_\alpha (\rho u^\alpha) = 0, \quad (8)$$

$$\nabla_\alpha T^{\alpha\beta} = 0, \quad (9)$$

$$\nabla_\alpha T_r^{\alpha\beta} = -G_r^\beta. \quad (10)$$

While equations (8) and (9) represent the well-known continuity equation and the energy momentum equation, equation (10) expresses the evolution of the radiation field, where G_r^α is the radiation four-force density. The latter depends on the physical interaction between matter and radiation and is therefore specific to the problem considered. In full generality this tensor is given by (Mihalas & Mihalas 1999; Shapiro 1996)

$$G_r^\alpha = \frac{1}{c} \int (\chi_\nu I_\nu - \eta_\nu) N^\alpha dv d\Omega, \quad (11)$$

where $\chi_\nu \equiv \chi_\nu^t + \chi_\nu^s$ and $\eta_\nu \equiv \eta_\nu^t + \eta_\nu^s$ are the total opacity and emissivity coefficients,³ each containing a thermal contribution, indicated with the superscript ‘t’, and a scattering one, indicated

with a superscript ‘s’. In addition, we assume that: (i) the scattering is isotropic and coherent; (ii) the thermal emissivity and the thermal opacity coefficients are related to the Planck function \tilde{B}_ν through Kirchhoff’s law $\eta_\nu^t = \tilde{B}_\nu \chi_\nu^t$; (iii) electrons and ions are maintained at the same temperature; (iv) the opacity coefficients are independent of frequency, $\chi_\nu = \kappa_g \rho$, where κ_g is the grey-body opacity. The last assumption, in particular, prevents us from taking into account photoionization effects, which are therefore not considered in our analysis.

Under these conditions, which are indeed the same considered by Farris et al. (2008), the radiation four-force can be written in covariant form as

$$G_r^\alpha = \chi^t (E_r - 4\pi \tilde{B}) u^\alpha + (\chi^t + \chi^s) F_r^\alpha, \quad (12)$$

where $4\pi \tilde{B} = a_{\text{rad}} T^4$ is the equilibrium black-body intensity, with T the temperature of the fluid and a_{rad} the radiation constant. The temperature is estimated from the ideal-gas EOS via the expression

$$T = \frac{m_p P}{k_B \rho}, \quad (13)$$

where, we recall, k_B is the Boltzmann constant and m_p the rest mass of the proton. In this paper we consider the case of bremsstrahlung opacity (Rybicki & Lightman 1986)

$$\begin{aligned} \chi_{\text{br}}^t &= 1.7 \times 10^{-25} T_K^{-7/2} Z^2 n_e n_i \text{ cm}^{-1} \\ &= 1.7 \times 10^{-25} T_K^{-7/2} \frac{\rho_{\text{cgs}}^2}{m_p^2} \text{ cm}^{-1}, \end{aligned} \quad (14)$$

where n_e and $n_i \simeq n_e$ are, respectively, the number densities of electrons and ions (protons) expressed in cgs units, while T_K is the equilibrium temperature of both electrons and protons expressed in Kelvin. For the scattering opacity we consider the Thomson scattering opacity and recall that the Thomson cross-sections of electrons and protons are: $\sigma_{\text{T,e}} = 6.6524586 \times 10^{-25} \text{ cm}^2$ and $\sigma_{\text{T,p}} = (m_e/m_p)^2 \sigma_{\text{T,e}}$, respectively. Hence, the Thomson scattering opacities of electrons and protons are given by

$$\chi_e^s = \sigma_{\text{T,e}} n_e = \sigma_{\text{T,e}} \left(\frac{\rho}{m_p} \right) = 0.397726 \rho_{\text{cgs}} \text{ cm}^{-1}, \quad (15)$$

$$\chi_p^s = \sigma_{\text{T,p}} n_p = \sigma_{\text{T,p}} \left(\frac{\rho}{m_p} \right) = 1.17968 \times 10^{-7} \rho_{\text{cgs}} \text{ cm}^{-1}. \quad (16)$$

We recall that the electron-scattering opacity dominates over free-free opacity at low densities and high temperatures (Harwit 1998), where the interaction between electrons and ions is weak. It is worth stressing that, because of the assumptions made, an incoherent process such as Compton scattering, with a cross-section that is frequency dependent, cannot be consistently taken into account and it is therefore neglected. Finally, as customary, the optical thickness is defined as the line integral of the opacities between two points in the fluid

$$\tau = \int_0^L (\chi^t + \chi^s) ds. \quad (17)$$

In practice, we approximate expression (17) as $\tau \simeq (\chi^t + \chi^s)L$, with L being a typical length-scale of the problem.

We refer to Appendix A for a summary about the conversion between cgs and geometrized units.

2.2 Numerical methods

We solve the equations of general-relativistic non-dissipative radiation hydrodynamics (8)–(10) through a modified version of the

³ Note that although both are referred to as ‘coefficients’, χ_ν and η_ν have different units. The dimensions of χ_ν are cm^{-1} , while those of η_ν are $\text{erg cm}^{-3} \text{ s}^{-1} \text{ Hz}^{-1} \text{ sr}^{-1}$.

ECHO code (Del Zanna et al. 2007), which adopts a 3 + 1 split of space–time in which the space–time is foliated into non-intersecting space-like hyper-surfaces Σ_t , defined as isosurfaces of a scalar time function t . Within this approach, the metric is decomposed according to (Arnowitt, Deser & Misner 1962)

$$ds^2 = -\alpha^2 dt^2 + \gamma_{ij} (dx^i + \beta^i dt)(dx^j + \beta^j dt), \quad (18)$$

where α is the lapse function, β^i is the shift vector, γ_{ij} is the spatial metric tensor, and

$$n_\mu = -\alpha \nabla_\mu t = (-\alpha, 0_i), \quad (n_\mu n^\mu = -1), \quad (19)$$

is the future-pointing time-like unit vector normal to the slices Σ_t . The observer moving with four-velocity $n^\mu = \{1/\alpha, -\beta^i/\alpha\}$ is called *Eulerian* (Smarr & York 1978). Any vector V^μ (or similarly a tensor) may be projected in its temporal component $V^{\hat{n}} = -n_\mu V^\mu$ and spatial component $\perp V^\mu = (g^\mu_\nu + n^\mu n_\nu)V^\nu$. As a result, any spatial vector V^μ (or tensor) must necessarily have a vanishing contravariant temporal component $V^t = 0$, whereas its covariant temporal component is $V_t = g_{t\mu} V^\mu = \beta_i V^i$, in general different from zero. The 3 + 1 splitting procedure just described can be applied to the vectors and tensor introduced so far to yield

$$u^\alpha = \Gamma n^\alpha + \Gamma v^\alpha, \quad (20)$$

$$T_m^{\alpha\beta} = W^{\alpha\beta} + S^\alpha n^\beta + n^\alpha S^\beta + U n^\alpha n^\beta, \quad (21)$$

$$F_r^\alpha = \alpha F_r^t n^\alpha + f_r^\alpha, \quad (22)$$

$$T_r^{\alpha\beta} = R_r^{\alpha\beta} + S_r^\alpha n^\beta + n^\alpha S_r^\beta + U_r n^\alpha n^\beta, \quad (23)$$

where all the tensors v^μ , $W^{\mu\nu}$, S^μ , f_r^μ , $R_r^{\mu\nu}$, S_r^μ correspond to the familiar three-dimensional quantities as measured by the Eulerian observers, are purely spatial and have indices that are raised and lowered by the spatial metric γ_{ij} . In particular, the newly introduced quantities are related to the corresponding quantities in the comoving frame by

$$D \equiv \rho \Gamma, \quad (24)$$

$$W^{ij} \equiv \rho h \Gamma^2 v^i v^j + p \gamma^{ij}, \quad (25)$$

$$S^i \equiv \rho h \Gamma^2 v^i, \quad (26)$$

$$U \equiv \rho h \Gamma^2 - p, \quad (27)$$

$$R_r^{ij} \equiv \frac{4}{3} E_r \Gamma^2 v^i v^j + \Gamma (f_r^i v^j + f_r^j v^i) + \mathcal{P}_r \gamma^{ij}, \quad (28)$$

$$S_r^i \equiv \frac{4}{3} E_r \Gamma^2 v^i + \Gamma (\alpha F_r^t v^i + f_r^i), \quad (29)$$

$$U_r \equiv \frac{4}{3} E_r \Gamma^2 + 2\alpha \Gamma F_r^t - \frac{E_r}{3}. \quad (30)$$

A few comments about the quantities in the equations above can be useful. The vectors v^i and f_r^i are the velocity and the radiation flux, respectively, as measured by the Eulerian observers, while $\Gamma = (1 - v^2)^{-1/2} = \alpha u^t$ is the Lorentz factor of the bulk flow. In particular, the radiation flux vector is $f_r^i = F_r^i + \beta^i F_r^t$ where F_r^t is computed from the orthogonality condition $F_r^\alpha u_\alpha = 0$ and is given by

$$F_r^t = \frac{v_i F_r^i}{\alpha - \beta_i v^i} = \frac{v_i f_r^i}{\alpha}. \quad (31)$$

It is interesting to note that $U_r = T_R^{\alpha\beta} n_\alpha n_\beta$ is the radiation energy density as measured by the Eulerian observers, in analogy with what

happens for the conserved energy density of the fluid U defined by (27).

The general-relativistic radiation-hydrodynamic equations are then written in the following conservative form:

$$\partial_t \mathcal{U} + \partial_i \mathcal{F}^i = \mathcal{S}, \quad (32)$$

which is appropriate for numerical integration via standard high-resolution shock-capturing (HRSC) methods developed for the Euler equations. The conservative variables and the corresponding fluxes in the i -direction are respectively given by

$$\mathcal{U} \equiv \sqrt{\gamma} \begin{bmatrix} D \\ S_j \\ U \\ (S_r)_j \\ U_r \end{bmatrix}, \quad \mathcal{F}^i \equiv \sqrt{\gamma} \begin{bmatrix} \alpha v^i D - \beta^i D \\ \alpha W^i_j - \beta^i S_j \\ \alpha S^i - \beta^i U \\ \alpha R_r^{ij} - \beta^i (S_r)_j \\ \alpha S_r^i - \beta^i U_r \end{bmatrix}, \quad (33)$$

whereas the sources, in any stationary background metric, can be written as

$$\mathcal{S} \equiv \sqrt{\gamma} \begin{bmatrix} 0 \\ \frac{1}{2} \alpha W^{ik} \partial_j \gamma_{ik} + S_i \partial_j \beta^i - U \partial_j \alpha + \alpha (G_r)_j \\ \frac{1}{2} W^{ik} \beta^j \partial_j \gamma_{ik} + W_i^j \partial_j \beta^i - S^j \partial_j \alpha + \alpha^2 G_r^t \\ \frac{1}{2} \alpha R_r^{ik} \partial_j \gamma_{ik} + (S_r)_i \partial_j \beta^i - U_r \partial_j \alpha - \alpha (G_r)_j \\ \frac{1}{2} R_r^{ik} \beta^j \partial_j \gamma_{ik} + (R_r)_i^j \partial_j \beta^i - S_r^j \partial_j \alpha - \alpha^2 G_r^t \end{bmatrix}, \quad (34)$$

where only purely spatial quantities are present. We note that $\sqrt{\gamma} \equiv \sqrt{-g}/\alpha$ is the determinant of the spatial metric. In our setup for two-dimensional simulations presented in Section 4 we assume the metric given by the Kerr solution with the limiting case of Schwarzschild metric for vanishing black hole spins.

The radial numerical grid is discretized by choosing N_r points from r_{\min} to r_{\max} , non-uniformly distributed according to the following scheme:

$$r_i = r_{\min} + a_1 \tan(a_2 x_i), \quad (35)$$

$$x_i = (\tilde{r}_i - r_{\min}) / (r_{\max} - r_{\min}), \quad (36)$$

where $a_1 = (r_{\max} - r_{\min})/a_0$, $a_2 = \arctan a_0$, while \tilde{r}_i are the coordinate points of the uniform grid from r_{\min} to r_{\max} . In practice, the free parameter a_0 controls the extent to which the grid points of the original uniform grid are concentrated towards r_{\min} , and we have chosen a_0 in the range [5–10] in most of our simulations. The angular grid is taken to be uniform.

The set of hydrodynamic equations is discretized in time with the method of lines and the evolution is performed with a second-order-modified Euler scheme. A fifth-order finite-difference algorithm based on an upwind monotonicity-preserving filter is employed for spatial reconstruction of primitive variables, whereas a two-wave HLL Riemann solver is used to ensure the shock-capturing

Table 1. Description of the initial states in the shock-tube tests with radiation field. The different columns refer respectively to: the test considered, the radiation constant, the adiabatic index and the thermal opacity. Also reported are the rest-mass density, pressure, velocity and radiation energy density in the ‘left’ (L) and ‘right’ (R) states.

Model	γ	a_{rad}	κ_{g}^f	ρ_{L}	p_{L}	u_{L}^x	$E_{\text{r,L}}$	ρ_{R}	p_{R}	u_{R}^x	$E_{\text{r,R}}$
1	5/3	1.234×10^{10}	0.4	1.0	3.0×10^{-5}	0.015	1.0×10^{-8}	2.4	1.61×10^{-4}	6.25×10^{-3}	2.51×10^{-7}
2	5/3	7.812×10^4	0.2	1.0	4.0×10^{-3}	0.25	2.0×10^{-5}	3.11	0.04512	0.0804	3.46×10^{-3}
3	2	1.543×10^{-7}	0.3	1.0	60.0	10.0	2.0	8.0	2.34×10^3	1.25	1.14×10^3
4	5/3	1.388×10^8	0.08	1.0	6.0×10^{-3}	0.69	0.18	3.65	3.59×10^{-2}	0.189	1.3

properties (see Del Zanna et al. 2007 for further details). As a final remark we note that as customary in HRSC methods, we introduce a tenuous and static ‘atmosphere’ in the regions of the fluid where the rest-mass density falls below a chosen threshold value. When this happens, we follow the prescription detailed in Baiotti et al. (2005) as far as the hydrodynamical quantities are concerned, while the primitive variables of the radiation field are frozen to the values at previous time-step.

3 VALIDATION OF THE CODE

The purely hydrodynamic version of the code has been validated over the same numerical tests extensively described in Del Zanna et al. (2007), obtaining the same convergence properties and will not be reported here for compactness. For the radiation part of the code, on the other hand, there are only a few analytic or semi-analytic tests that can be adopted, as we discuss below.

3.1 Shock-tube problems

Considering a flat space–time, we have followed Farris et al. (2008), who proposed and solved four shock-tube tests in which non-linear radiation-hydrodynamic waves propagate. The initial states of these tests are reported in Table 1 and are chosen in such a way that the discontinuity front at $x = 0$ remains stationary, namely it has zero velocity with respect to the Eulerian observer of the code. The values of the fluxes, not reported in Table 1, are chosen to be two orders of magnitude smaller than the energy density of the radiation field. In these tests local thermodynamic equilibrium is assumed at both ends $x = \pm X$, with $X = 20$, and this is obtained by adopting a fictitious value of the radiation constant a_{rad} , namely $a_{\text{rad}} = E_{\text{r,L}}/T_{\text{L}}^4$, which is then used to compute $E_{\text{r,R}} = a_{\text{rad}}T_{\text{R}}^4$ (here the indices L and R indicate the ‘left’ and ‘right’ states, respectively). The scattering opacity κ_{g}^s is set to zero in all of the tests, while the value of the thermal opacity κ_{g}^f is reported in Table 1.

Each test is evolved in time until stationarity is reached. The semi-analytic solution that is used for comparison with the numerical one has been obtained following the strategy by Farris et al. (2008), and it implies the solution of the following system of ordinary differential equations

$$d_x \mathbf{U}(\mathbf{P}) = \mathbf{S}(\mathbf{P}),$$

where

$$\mathbf{P} = \begin{pmatrix} \rho \\ P \\ u^x \\ E_{\text{r}} \\ F_{\text{r}}^x \end{pmatrix}, \quad \mathbf{U} = \begin{pmatrix} \rho u^x \\ T^{0x} \\ T^{xx} \\ T_{\text{r}}^{0x} \\ T_{\text{r}}^{xx} \end{pmatrix}, \quad \mathbf{S} = \begin{pmatrix} 0 \\ 0 \\ 0 \\ -G_{\text{r}}^0 \\ -G_{\text{r}}^x \end{pmatrix}.$$

Figs 1 and 2 show the comparison of the numerical solution with respect to the semi-analytic one in the four cases considered, which correspond, respectively, to the propagation of a non-relativistic strong shock, of a mildly relativistic strong shock, of a highly relativistic wave and of a radiation-pressure-dominated mildly relativistic wave. In particular, Fig. 1 reports the solution for the tests 1 and 2, which contain a true discontinuity represented by a shock front, while tests 3 and 4 have continuous configurations and are shown in Fig. 2.

The tests have been performed with $N = 800$ uniformly spaced grid points using the MP5 slope limiter described in Del Zanna et al. (2007) and a HLL Riemann solver. Unlike Farris et al. (2008), we have not boosted the solution. This results in a more stringent test for the code to maintain stationarity and it also explains why the profiles of the vector quantities, namely the velocity and the radiation flux, do not match those shown by Farris et al. (2008). The numerical solution is almost indistinguishable from the semi-analytic one in all of the profiles reported in the figures, thus proving the ability of the code in handling different physical regimes of the radiation field within an optically thick approximation.

4 BONDI–HOYLE ACCRETION FLOWS

4.1 Initial and boundary conditions

Our attention is focused on a Bondi–Hoyle accretion flow on to a black hole of galactic size with $M_{\text{BH}} = 3.6 \times 10^6 M_{\odot}$, that we investigate by performing numerical simulations on the equatorial plane, i.e. $\theta = \pi/2$. Despite the long history in literature on this type of accretion (see the review by Edgar 2004), no stationary solution for a radiation-hydrodynamic Bondi–Hoyle flow is known, which could have been used as suitable initial data. As a result, we let the code converge to the nearest stationary solution after specifying the hydrodynamical solution of the Bondi–Hoyle flow, to which we add a radiation field with uniform and small energy density E_{r} .

Most of our discussion hereafter refers to accretion on to Schwarzschild black holes, although also rotating black holes will be briefly presented in Section 4.3.3. The code solves therefore the equations in a general Kerr metric expressed in Boyer–Lindquist coordinates, so that the initial velocity field, specified in terms of an asymptotic velocity v_{∞} , is given by (Font & Ibáñez 1998)

$$v^r = \sqrt{\gamma^{rr}} v_{\infty} \cos \phi, \quad (37)$$

$$v^{\phi} = -\sqrt{\gamma^{\phi\phi}} v_{\infty} \sin \phi. \quad (38)$$

These relations guarantee that the velocity of the injected gas at infinity is parallel to the x -direction, while $v^2 \equiv v_i v^i = v_{\infty}^2$ everywhere in the flow. Other quantities that need to be set initially are: the asymptotic sound speed $c_{\text{s},\infty}$, and the asymptotic pressure, from which the asymptotic rest-mass density ρ_{∞} follows directly

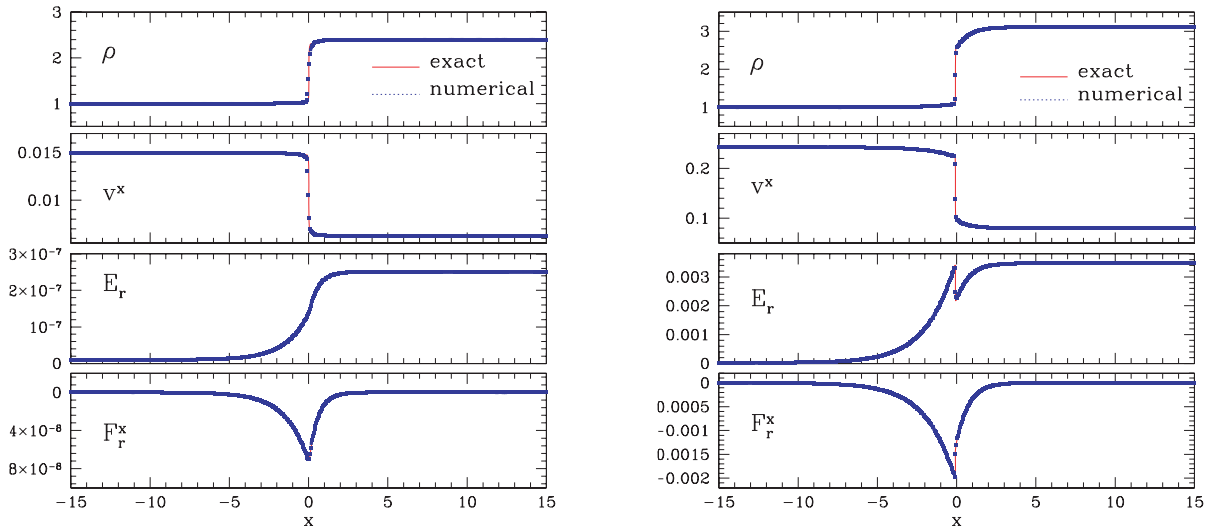


Figure 1. Solution of the shock tube test 1 (left-hand panel) and 2 (right-hand panel) as reported in Table 1. From top to bottom the panels report the rest-mass density, the velocity, the radiation energy density and the radiation flux.

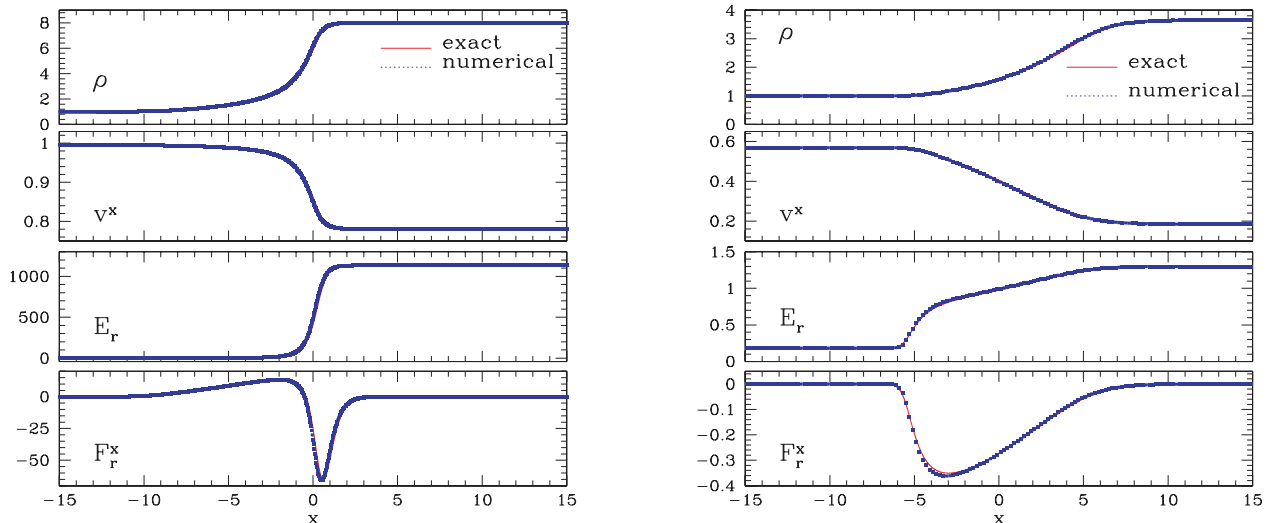


Figure 2. Solution of the shock tube test 3 (left-hand panel) and 4 (right-hand panel) as reported in Table 1. From top to bottom the panels report the rest-mass density, the velocity, the radiation energy density and the radiation flux.

(see values reported in Table 2 for all of the models considered). For all the simulations we will consider a gas of non-relativistic electrons and hence with an adiabatic index $\gamma = 5/3$. The velocities used in our models and presented in Table 2 are chosen to be sufficiently high so as to open a shock cone (see details below). Any chosen v_∞ implies a restricted range of asymptotic sound speeds, if a reasonable Mach number should be considered. We remark that our models do not aim at modelling any specific astrophysical scenario, but rather at highlighting the role of the back-reaction of the radiation in an optically thick, relativistic Bondi–Hoyle accretion flow.

Similarly, the radiation field is initialized to a value such that the radiation temperature $T_{\text{rad}} = (E_r/a_{\text{rad}})^{1/4} \approx 1.5 \times 10^5$ K. While this may seem an arbitrary choice, we have verified through a series of numerical simulations that, on long-term evolutions, the value of the obtained luminosity is not dependent of this initial choice. The computational grid consists of $N_r \times N_\phi$ numerical cells in the

radial and angular directions, respectively, covering a computational domain extending from $r_{\text{min}} = 2.1 M$ to $r_{\text{max}} = 200 M$ and from $\phi_{\text{min}} = 0$ to $\phi_{\text{max}} = 2\pi$. For our fiducial simulation we have chosen $N_r = 1536$ and $N_\phi = 300$, but have also verified that the results are not sensitive to the resolution used or to the location of the outer boundary.

The boundary conditions in the radial direction are such that at the inner radial grid point we implement inflow boundary conditions by a simple zeroth-order extrapolation (i.e. a direct copy) of all variables. We have verified that such conditions effectively prevent inflow of matter from the region below r_{min} . At the outer radial boundary, on the other hand, we must distinguish between the upstream region (i.e. with $\pi/2 < \phi < 3/2\pi$), and the downstream region (i.e. with $-\pi/2 < \phi < \pi/2$). In the upstream region we continuously inject matter with the initial velocity field of (37)–(38), thus reproducing a continuous wind at large distances, while in the downstream region we use outflow boundary conditions. Finally,

Table 2. Initial models adopted in numerical simulation. From left to right the columns report: the name of the model, the asymptotic flow velocity v_∞ , the asymptotic sound speed $c_{s,\infty}$, the asymptotic Mach number \mathcal{M}_∞ , the initial temperature, the initial rest-mass density and the accretion radius $r_a \equiv GM/(v_\infty^2 + c_{s,\infty}^2)$. Perturbed Bondi–Hoyle solutions are generated through injection of low pressure gas as described in the text. Each model is evolved until stationarity is reached, and in any case up until at least $t = 20\,000 M$. The adiabatic index was set to $\gamma = 5/3$ and the black hole spin $a = 0$. The mass of the black hole is $M_{\text{BH}} = 3.6 \times 10^6 M_\odot$ and the radial grid extends from $r_{\text{min}} = 2.1 M$ to $r_{\text{max}} = 200 M$.

Model	v_∞	$c_{s,\infty}$	\mathcal{M}_∞	T (K)	ρ_∞ (cgs)	r_a (M)
V08.CS07	0.08	0.07	1.14	3.22×10^{10}	3.22×10^{-12}	88.5
V09.CS07	0.09	0.07	1.28	3.22×10^{10}	3.22×10^{-12}	76.9
V10.CS07	0.10	0.07	1.42	3.22×10^{10}	3.22×10^{-12}	67.1
V11.CS07	0.11	0.07	1.57	3.22×10^{10}	3.22×10^{-12}	58.8
V07.CS06	0.07	0.06	1.16	2.36×10^{10}	4.39×10^{-12}	117.6
V07.CS07	0.07	0.07	1.0	3.22×10^{10}	3.22×10^{-12}	102.0
V07.CS08	0.07	0.08	0.77	4.22×10^{10}	2.45×10^{-12}	88.5
V07.CS09	0.07	0.09	0.77	5.35×10^{10}	1.93×10^{-12}	76.9
p.V09.CS07	0.09	0.07	1.28	3.22×10^9	3.22×10^{-12}	76.9
p.V10.CS07	0.10	0.07	1.42	3.22×10^9	3.22×10^{-12}	67.1
p.V11.CS07	0.11	0.07	1.57	3.22×10^9	3.22×10^{-12}	58.8
p.V18.CS07	0.18	0.07	2.57	3.22×10^9	3.22×10^{-12}	26.8

symmetric (i.e. periodic) boundary conditions are adopted at $\phi = 0$. The simulations are performed with a Courant–Friedrichs–Lewy coefficient that may vary according to the model and is typically in the range $\sim [0.01, 0.5]$.

In addition to the ‘classical’ Bondi–Hoyle initial data, we will also consider a set of simulations in which the thermodynamics of the flow is slightly altered in order to reduce the temperature of the gas. We denote these models as ‘p-models’ in Table 2. In essence, the perturbed Bondi–Hoyle accretion flows are obtained by injecting gas of lower pressure than required by the stationary solution at the upwind boundary, with a proportionally reduced radiation energy density E_r (see Section 4.3.2 for details).

4.2 Computation of luminosity

The key new quantity that our code allows us to compute is the emitted luminosity. Since the code explicitly calculates the radiation fluxes f_r^i at each time-step, we use them to compute the intrinsic luminosity emitted from the optically thick region as

$$L = \int_{\Omega} f_r^i n_i \, dS_{\text{opt}}, \quad (39)$$

where S_{opt} is the surface of the volume Ω enclosing an optically thick region within the computational domain, while the scalar product $f_r^i n_i$ provides the projection of the local radiation flux on to the normal to the radiating surface. Because of the nearly isotropic assumption made for the radiation field and because of the rough spherical symmetry of the physical system under consideration, the fluxes in the angular directions are expected to be much smaller than the radial ones and to almost cancel. As a result, and for simplicity, we approximate the scalar product above as $f_r^i n_i = f_r^r$, thus computing the luminosity as

$$L = 2 \sum_{n=1}^{N_\phi} [\sqrt{\gamma} (f_r^r)_n \Delta\phi_n] |_{\tau=1}, \quad (40)$$

where $\Delta\phi_n$ is the angular size of a grid cell and we perform the surface integral at the radial position of the last optically thick surface, i.e. where $\tau = 1$; the factor 2 accounts for both the contributions above and below the equatorial plane.

The luminosity computed in this way comprises two different contributions. The first one is an accretion-powered luminosity that is directly proportional to the mass-accretion rate \dot{M} through a relation of the type $L_{\text{acc}} = \eta \dot{M}$, where the coefficient η expresses the efficiency of the conversion of gravitational binding energy into radiation. The main dissipative mechanism is provided by compression of the fluid when this has non-zero thermal conductivity.⁴ A second contribution to the total luminosity (40) is given by dissipative processes related to shock heating that, as we will show below, can provide a considerable contribution to the total emission.

However, since we are dealing with inviscid non-magnetized fluids, the luminosity (40) obviously cannot provide the contribution coming from dissipative processes driven by viscosity (of whatever origin), and that can be a significant part of the accretion-powered luminosity in a realistic accretion scenario. We recall, for instance, that in the classical Shakura–Sunyaev thin-disc model the main dissipative mechanism comes from the viscous stress tensor, directly proportional to the total pressure via the ‘alpha’ parameter. Similarly, in spherical accretion, a realistic viscous fluid with non-zero bulk viscosity will produce a viscous dissipation adding to the one coming from the fluid compression. In summary, in realistic accretion scenarios one should expect that *both* thermal conductivity and viscosity act as transport coefficients of dissipative processes and lead to contributions to the emitted luminosity. In our treatment, however, only the effects of the former one can be accounted for. Hereafter, the luminosities and the accretion rates will be reported in Eddington units, i.e. $L_{\text{Edd}} = 4\pi G M m_p c / \sigma_{\text{T,e}} \simeq 1.26 \times 10^{38} (M/M_\odot) \text{ erg s}^{-1}$, $\dot{M}_{\text{Edd}} = L_{\text{Edd}}/c^2 \simeq 1.39 \times 10^{17} (M/M_\odot) \text{ g s}^{-1}$. See also (A8) for the Eddington luminosity in the geometrized units of the code.

4.3 Results

Before entering into the details of our results, it is useful to briefly review the main features of the relativistic Bondi–Hoyle accretion as

⁴ We recall that the thermal conductivity is related to the opacity and its effects are therefore accounted for in our analysis. For instance, the thermal conductivity computed using the ordinary diffusion approximation of stellar interiors is given by $\chi_{\text{T}} = (4/3)a_{\text{rad}}cT^3/\chi^s$ (Schwartz 1967).

investigated through purely hydrodynamical simulations by Petrich et al. (1989), Font & Ibáñez (1998), Font, Ibáñez & Papadopoulos (1998) and Font, Ibáñez & Papadopoulos (1999). Overall, these studies have highlighted that when a homogeneous flow of matter moves non-radially towards a compact object, a shock wave will form close to the accretor. Depending on the adiabatic index and on the asymptotic Mach number⁵ \mathcal{M}_∞ , the shock can either come very close to the accretor or be at a certain distance from it (see e.g. Foglizzo, Galletti & Ruffert 2005). In general, for any given value of the adiabatic index, there is a minimum asymptotic Mach number above which a shock wave of conic shape, i.e. a ‘*shock cone*’, forms downstream of the accretor. On the other hand, asymptotic Mach numbers below the critical value produce a shock wave that, initially formed in the downstream region, opens progressively and reverses in the upstream region as a bow shock. More recently, two different studies have shed additional light on the physics of relativistic Bondi–Hoyle accretion flows. In the first one, Dönmez, Zanotti & Rezzolla (2010) reported the occurrence of the so-called *flip-flop* instability of the shock cone in the relativistic regime and have also shown that quasi-periodic oscillations of sonic nature are produced in the shock cone. In the second one, Penner (2011) investigated the effects of a uniform magnetic field, finding that it produces an increase in the cone opening angle and in the mass accretion rate.

4.3.1 Classical Bondi–Hoyle accretion

We start our analysis by considering the extent to which a radiation field affects the dynamics of the classical Bondi–Hoyle flow, comparing the dynamics for very similar physical conditions. The initial models, which are the first seven reported in Table 2, have very high temperatures and, consequently, high thermal conductivities.⁶ As mentioned above, for any given value of the adiabatic index, there is a critical asymptotic Mach number $\mathcal{M}_{\infty,c}$, usually close to unity, above which a shock cone forms in the downstream region and below which the shock cone reverses in the upstream region. Our simulations indicate that, for values of the Mach number close to the critical one, the radiation effects on the dynamics are most evident. This is shown in Fig. 3 for model V09.CS07, where we have reported the distribution of the rest-mass density at three different times in a purely hydrodynamical evolution (left-hand panels) and in a radiation-hydrodynamic evolution (right-hand panels). This model, in particular, provides an example in which the radiation field prevents the reversal of the shock cone from the downstream region into the upstream region, which instead takes place in the purely hydrodynamical evolution. Since the dynamics of V09.CS07 becomes radiation pressure dominated around $t \sim 5000M$, the explanation of this effect is simple: in such conditions the effective adiabatic index of the fluid-plus-radiation medium is smaller than that of the fluid alone [see equation 70.22 of Mihalas & Mihalas (1999)]

$$\gamma_{\text{eff}} = \frac{5/2 + 20q + 16q^2}{(3/2 + 12q)(1 + q)}, \quad (41)$$

⁵ We recall that the relativistic Mach number is defined as $\mathcal{M} = \Gamma v / (c_s \Gamma_s)$, where Γ and Γ_s are the Lorentz factors of the flow and of the sound speed, respectively.

⁶ The present version of the code does not allow us to handle stiff source terms that arise in the radiation-hydrodynamic equations when the conductivity is small (Szöke et al. 2006). Work is in progress to cope with this difficulty.

where $q = \mathcal{P}_r/p$. This fact has two important consequences. The first one, which we will discuss shortly when commenting Fig. 7, is to increase the rest-mass density jumps across shock fronts. The second one is exactly to favour the generation of the shock cone downstream of the accretor, as first noticed by Ruffert (1996) and later confirmed by Font & Ibáñez (1998).

As clearly shown in Fig. 3, the radiation-hydrodynamic evolution of model V09.CS07 is remarkably different from the purely hydrodynamical one, and it can be divided in the following stages. After the shock cone has fully opened in the downstream region (top-right panel of Fig. 3), the flow becomes radiation-pressure dominated, making the shock cone oscillate from one side of the accretor to the other, in a way that resembles the flip-flop instability already encountered in relativistic Bondi–Hoyle flows by Dönmez et al. (2010). This transient behaviour, captured in the right-middle panel of Fig. 3, is accompanied by an outflow of matter expelled by radiation pressure beyond the computational grid. After that the system relaxes to a stationary configuration characterized by the presence of a shock cone with a much smaller opening angle than in the hydrodynamical solution, giving rise to a ‘reduced’ shock cone. Also shown in Fig. 4 is the ratio between the radiation pressure and the fluid pressure, reported in the left-hand panel for an early and fluid-pressure-dominated stage of the evolution, and in the right-hand panel for a late and radiation-pressure-dominated one.

A very similar behaviour to the one discussed so far is shown in Fig. 5 for model V10.CS07, the initial Mach number of which is only slightly larger than model V09.CS07. However, in this case the higher fluid velocity causes supercritical behaviour both in the hydrodynamical and in the radiation-hydrodynamic evolution so that the shock cone remains in the downstream region. The close similarity between the dynamics of models V09.CS07 and V10.CS07 in the presence of the radiation field is also testified by the asymptotic mass accretion rate, which is $\dot{M} \simeq 13.14\dot{M}_{\text{Edd}}$ for model V09.CS07 and $\dot{M} \simeq 10.24\dot{M}_{\text{Edd}}$ for V10.CS07.

An information complementary to that of Figs 3–5 is provided by Fig. 6, which shows the evolution of the mass accretion rate for a few selected models. For each of these models both the purely hydrodynamical evolution (red solid lines) and the radiation-hydrodynamical one (blue dashed lines) are considered. A few comments are worth making about this figure. The first one is that, once stationarity is reached, the mass accretion rates of the radiation-hydrodynamic models are significantly smaller than those of the corresponding hydrodynamics models. This result was of course expected, because of the obstructive effect of the radiation pressure. The second comment is that the reversal of the shock cone in the hydrodynamics models V09.CS07, V07.CS07, V07.CS09 and in the radiation-hydrodynamic models V07.CS07 and V07.CS09 leads to an increase of \dot{M} , as highlighted by the arrows. For the hydrodynamical version of model V09.CS07, for instance, this increase starts at $t \sim 12000M$, as reported in the top-left panel of Fig. 6. Finally, we find that all models accrete at super-Eddington rates even when a radiation field is present.⁷ This is not surprising, since the Eddington limit holds strictly only in spherical symmetry, which is not fulfilled in wind-like accretion. Moreover, it should be remarked that the classical Eddington limit is computed in a framework where

⁷ The fraction of matter accreted depends on the position of the shock front. When the shock forms in the downstream region, about 80–90 per cent of the matter crossing the shock front is accreted by the black hole. This percentage decreases to 50–60 per cent, when the matter crosses the shock front in the upstream region.

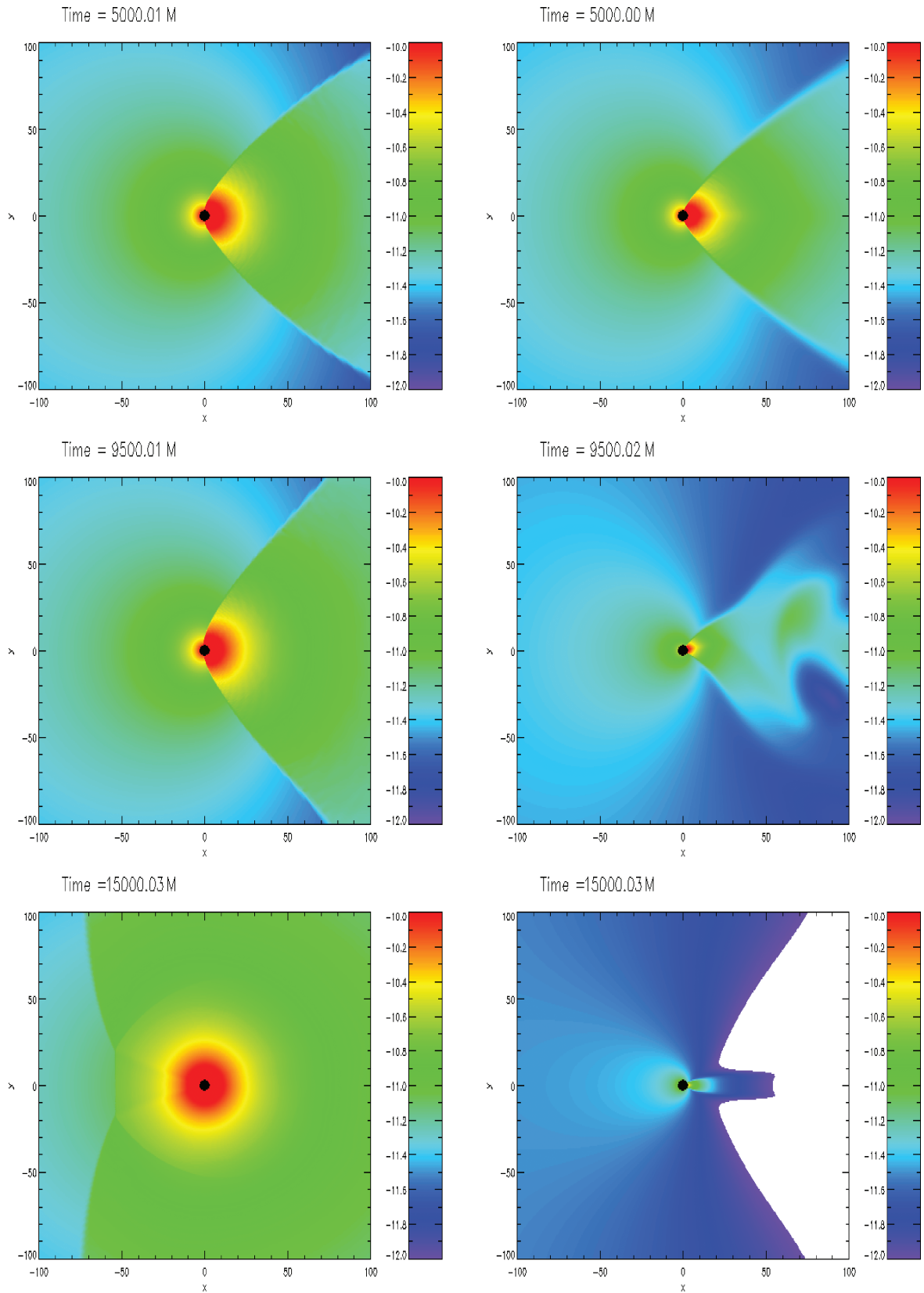


Figure 3. Rest-mass density in cgs units on a logarithmic scale for model V09.CS07 in a purely hydrodynamical evolution (left-hand panels) and in a radiation-hydrodynamic evolution (right-hand panels). Different rows refer to different times of the evolution and white regions correspond to densities slightly below the threshold for the colour code at around 10^{-12} g/cm⁻³. Note that the presence of a radiation field reduces the rest-mass density considerably near the black hole, suppressing the accretion rate.

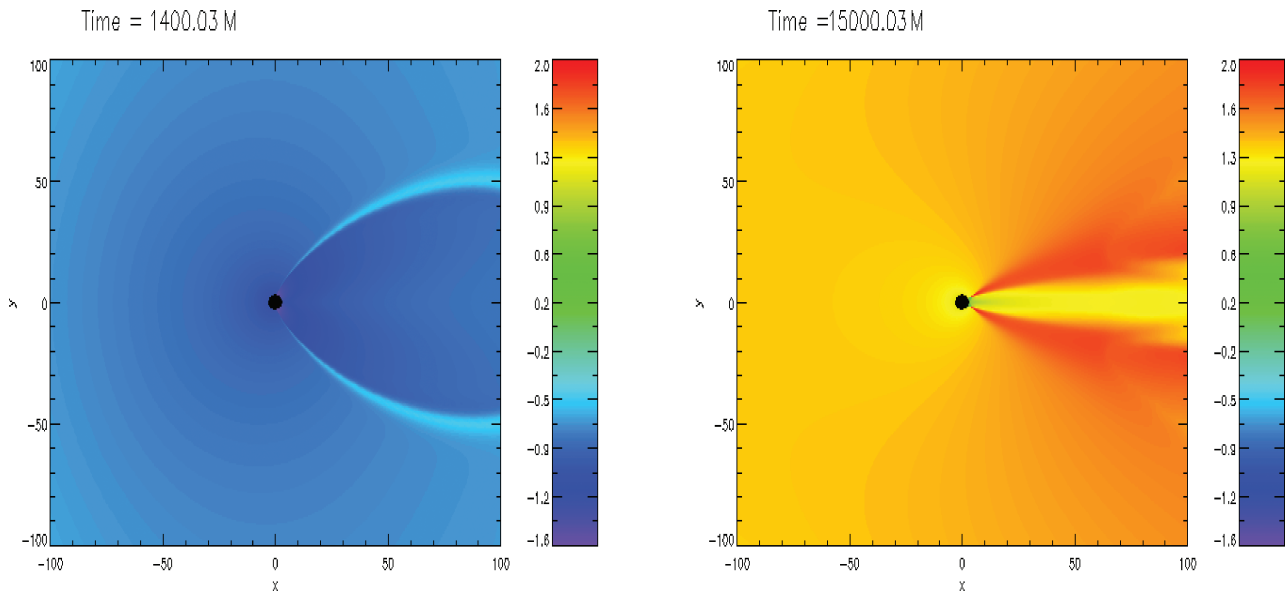


Figure 4. Left-hand panel: logarithm of the ratio of radiation pressure over gas pressure for the model V09.CS07 at early times. Right-hand panel: the same as the right-hand panel but at later times, when stationarity had been reached.

only the electron Thomson cross-section contributes to the radiation pressure.

Additional differences between the hydrodynamics and the radiation-hydrodynamic evolutions emerge after comparing the jumps experienced by the rest-mass density across a shock wave in a representative model. Such a comparison is reported in Fig. 7 for model V09.CS07, showing the variation of the rest-mass density across the shock that is produced at time $t = 5000M$ and visible in the two top panels of Fig. 3. The two curves have been obtained after slicing the rest-mass density along an ‘ x -direction’ perpendicular to the shock front, and sliding the two profiles so that the shock is located at the same $x = 0$ position for both the hydrodynamical and the radiation-hydrodynamical evolution. Negative and positive values of the x -coordinate refer therefore to the unshocked and to the shocked region, respectively, while the rest-mass density has been normalized to the value in the unshocked region.

The first comment about this figure is that the density jump in the hydrodynamics evolution is slightly smaller than the value of 4 predicted by the theoretical expectation of $\rho_2/\rho_1 \sim (\gamma + 1)/(\gamma - 1)$ valid for an ideal-gas EOS. This effect may be due to the presence of both numerical diffusion and tangential velocities along the shock front. The second comment is that the compression ratio across the shock increases by 3 per cent in the transition from a hydrodynamical to a radiation-hydrodynamical evolution. This effect can again be understood by regarding the fluid in the radiation-hydrodynamic evolution as an effective fluid having a *smaller* adiabatic index, as indeed expected in the radiation-pressure-dominated regime. This result is also in agreement with analytical investigations by Guess (1960) and Mihalas & Mihalas (1999) (section 104).

Before computing the luminosity as described in Section 4.2, it is important to make sure that the physical conditions chosen correspond to those required by the code, namely the presence (and the persistence) of an optically thick regime. Of course all of the models considered in our simulations and reported in Table 2 are in such a physical regime, with only very limited regions where the optical thickness can be $\sim \mathcal{O}(1)$ during the evolution. As a representative example, the left-hand panel of Fig. 8 shows the optical thickness when the system is relaxed to stationarity, for

the same model V09.CS07 that we have extensively described so far. The right-hand panel of Fig. 8, on the other hand, shows the corresponding intensity of the momentum of the radiation field. After comparing with the right-bottom panel of Fig. 3, it is easy to realize not only that the distribution of the radiative fluxes is obviously correlated with the rest-mass density distribution, but also that a good portion of the radiative emission is concentrated along the shock fronts of the reduced shock cone.

The evolution of the emitted luminosity and of the mass-accretion rates is illustrated in the two panels of Fig. 9. More specifically, the left-hand panel, which reports models with increasing Mach number but having the same initial temperature, shows that the luminosity increases with \mathcal{M}_∞ and reaches stationary values of a few Eddington units. On the other hand, the right-hand panel, which reports models with the same asymptotic velocity but different temperatures, shows that stationarity is reached on longer time-scales and a correlation with the final luminosity is less robust. In all of the models shown, the first bump around $t \sim 2000M$ is due to the initial opening of the shock cone.

By providing the first self-consistent computation of the luminosity in a Bondi–Hoyle accretion flow, our calculations allow us to derive the efficiency of the accretion flow $\eta_{B\mathcal{H}}$. We remark that the concept of $\eta_{B\mathcal{H}}$ for a Bondi–Hoyle flow, with a non-zero velocity of the matter at infinity, is not the same as in standard accretion discs, where the gas flow is supposed to start from matter at rest at infinity. Thus, we define an effective Bondi–Hoyle luminosity efficiency $\eta_{B\mathcal{H}}$ as

$$\eta_{B\mathcal{H}} = \frac{L}{\dot{M}_{\text{acc}}c^2 + \frac{1}{2}\dot{M}_\infty v_\infty^2}, \quad (42)$$

where the denominator takes into account a kinetic contribution to the energy flux. We report the values of $\dot{M}_{\text{acc}}/\dot{M}_{\text{Edd}}$, L/L_{Edd} and $\eta_{B\mathcal{H}}$ in Table 3 for those models presenting a quasi-stationary accretion pattern. From the data reported in the table it is possible to deduce the existence of two different regimes in a radiative Bondi–Hoyle accretion flow. A first regime corresponds to $\mathcal{M}_\infty \lesssim 1$, where the luminosity is dominated by the accretion-powered luminosity and thus is proportional to \dot{M} . A second regime

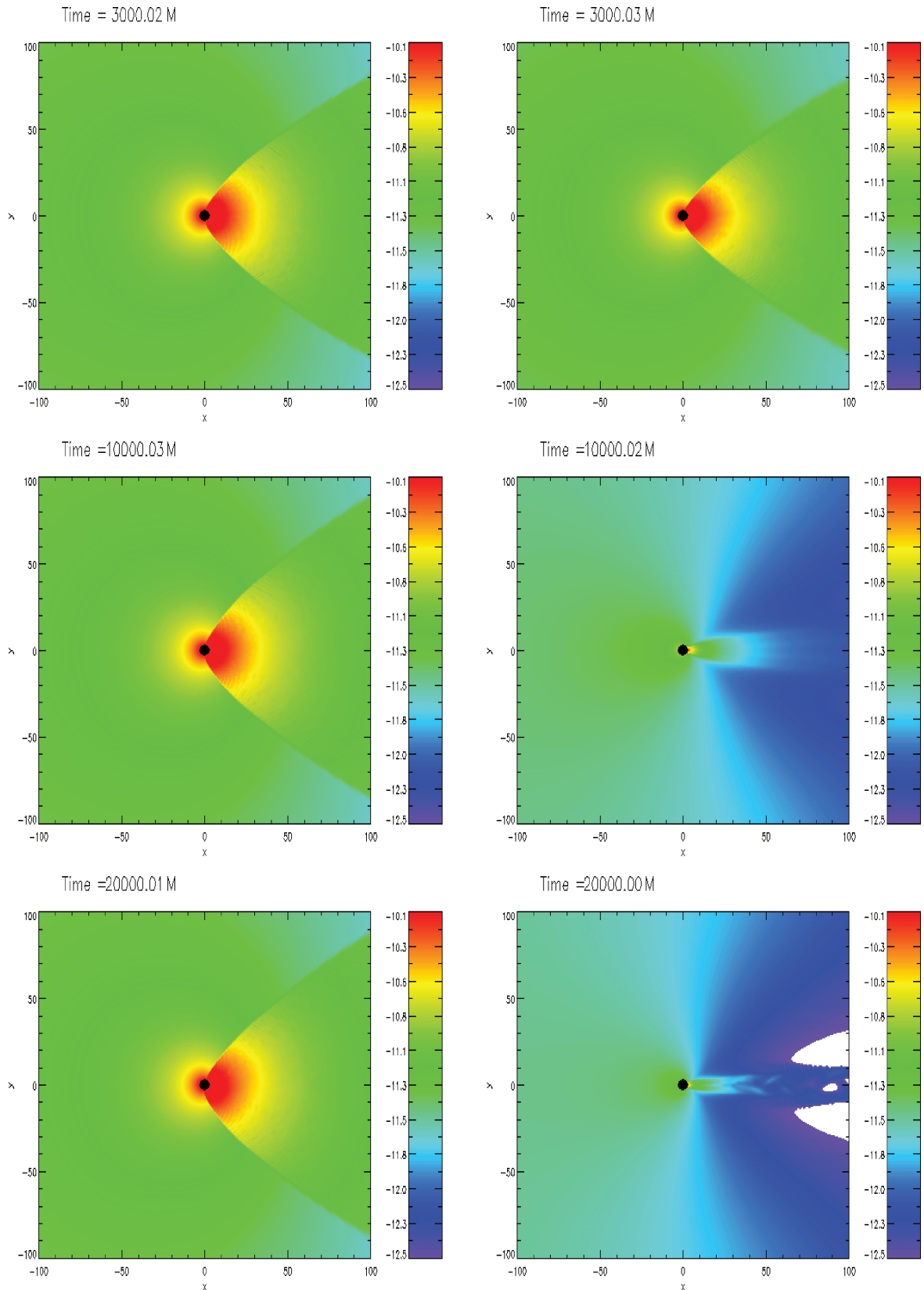


Figure 5. Rest-mass density in cgs units on a logarithmic scale for model V10.CS07 in a purely hydrodynamical evolution (left-hand panels) and in a radiation-hydrodynamic evolution (right-hand panels). Different rows refer to different times of the evolution and white regions correspond to densities slightly below the threshold for the colour code at around 10^{-12} g/cm $^{-3}$. Note that the presence of a radiation field reduces the rest-mass density considerably near the black hole, suppressing the accretion rate.

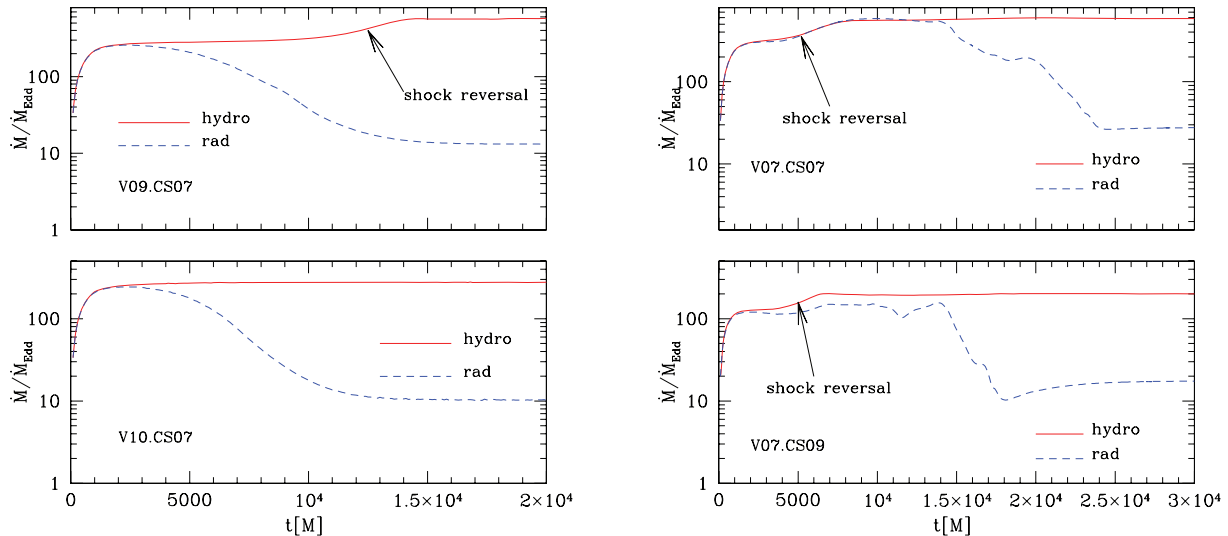


Figure 6. Evolution of the mass accretion rate in Eddington units for models V07.CS07 and V07.CS09 (left-hand panels) and V09.CS07 and V10.CS07 (right-hand panels).

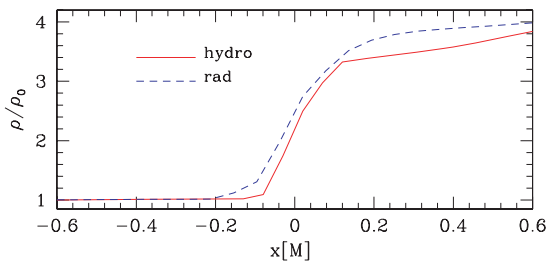


Figure 7. Comparison of the rest-mass density jump across the shock front at time $t = 5000$ for models V09.CS07 in a purely hydrodynamics evolution (red solid line) and in a radiation-hydrodynamic evolution (blue dashed line). The location of the shock was re-normalized to lie at $x = 0$ and is displaced by $\Delta x \sim 0.2M$ between the two runs.

corresponds to $\mathcal{M}_\infty \gtrsim 1$, where the luminosity is instead dominated by the emission at the shock front. In particular, by comparing the first four models that have the same initial asymptotic sound speed, we note that, as the asymptotic Mach number is increased, the accretion rates decrease. This effect is due to the reduced opening angle of the shock cone. The corresponding luminosity, on the other hand, increases, because of the enhanced dissipation at the shock front.

As a final remark we note that, as already discussed in Section 4.2, the luminosities we have reported here can only provide lower limits on the energy efficiency $\eta_{B\gamma L}$. We have in fact neglected not only viscous dissipative processes from the accretion flow, but also any non-thermal emission, such as inverse Compton or synchrotron radiation, which could arise from a corona developing near the black hole.

4.3.2 Perturbed Bondi–Hoyle flow

As mentioned in Section 4.1, in addition to the standard and stationary Bondi–Hoyle flows, we have also considered initial conditions that would lead to perturbed Bondi–Hoyle accretion patterns (we recall that we have tagged these as the ‘p-models’). The rationale behind this choice is that of investigating how the accretion flows vary when the initial conditions are no longer those ensuring a

stationary flow. At the same time, this allows us to consider models that have lower temperatures and, consequently, lower thermal conductivities.

In practice, we trigger the perturbation of the Bondi–Hoyle flow by acting on the thermodynamic conditions of the fluid in the upstream region and by producing models with values of the initial temperature that are typically one order of magnitude smaller than those in standard Bondi–Hoyle models. Because of the perturbation introduced, the dynamics of the perturbed models is typically characterized by a very dynamical phase before quasi-stationarity is reached. However, in spite of these violent transients, the perturbation introduced does not destroy the general Bondi–Hoyle pattern, which is recovered eventually.

Among the perturbed models, p.V09.CS07 has the minimum Mach number, and is also the only one producing a shock cone that progressively reverses into the upstream region as a bow shock. The remaining three models, which all have higher Mach numbers, develop the usual shock cone downstream of the black hole. This behaviour is reported in the four panels of Fig. 10, showing the evolution at different times of the rest-mass density for the model p.V10.CS07 in a radiation-hydrodynamical evolution. Note that the accretion cone, that is fully formed at time $t \sim 3000M$, is highly unstable and it goes through a rapid sequence of oscillations generating an undulated wake. Finally, the system reaches a quasi-equilibrium state characterized by a reduced shock cone similar to that already encountered in the dynamics of standard models.

The extraction of the light-curve and the computation of all remaining quantities follow the same procedure used in the standard models, and we have reported the mass-accretion rates and the light curves in the two panels of Fig. 11. Note that the general features in the light curves for the standard models are also present for the perturbed models. In particular, there is an initial rise in luminosity which corresponds to the formation of the shock cone. After that, between $t \sim 1000M$ and $t \sim 2000M$ depending on the model, a peak is produced in the light curve which is due to the shock cone changing its geometry to an open cone. Interestingly, even the efficiency $\eta_{B\gamma L}$ of the perturbed models are very similar to those of the corresponding standard ones. For the model p.V11.CS07, for instance, $\eta_{B\gamma L} = 0.40$, to be compared with $\eta_{B\gamma L} = 0.38$ of V11.CS07.

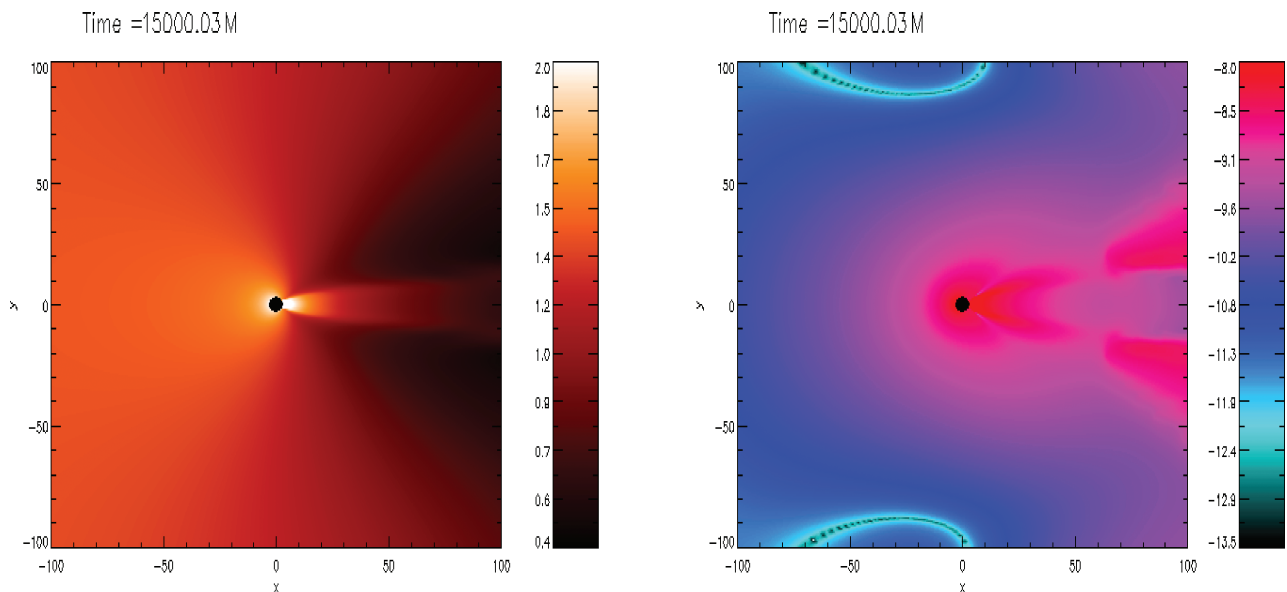


Figure 8. Left-hand panel: logarithm of the optical thickness for the model V09.CS07 once stationarity is reached. Right-hand panel: logarithm of the modulus of the radiative flux (in geometrized units) in the same model at the same time.

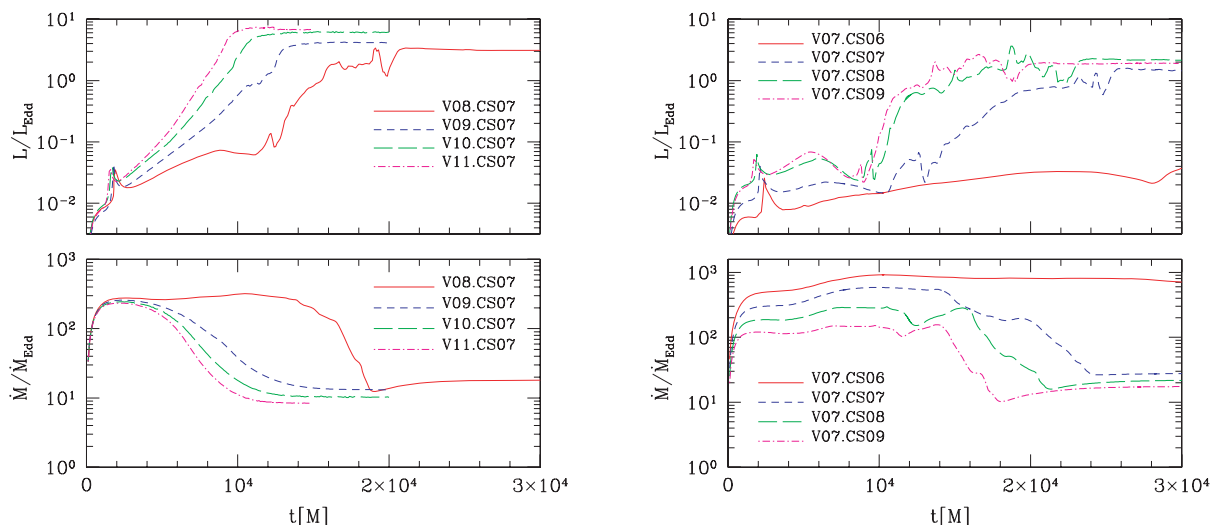


Figure 9. Luminosity and mass-accretion rates in Eddington units in classical Bondi–Hoyle accretion flows. The left-hand panel collects models with different initial velocities but with the same sound speed. In contrast, the right-hand panel collects models with the same initial velocities but with different values for the sound speed. All simulations were evolved until they reached stationarity, and up to $t = 30\,000 M$ at most.

Table 3. Mass accretion rate, luminosity and efficiency $\eta_{B\mathcal{H}}$ as defined in equation (42) of the Bondi–Hoyle accretion in the quasi-stationary regime.

Model	\mathcal{M}_∞	$\dot{M}_{\text{acc}}/\dot{M}_{\text{Edd}}$	L/L_{Edd}	$\eta_{B\mathcal{H}}$
V08.CS07	1.14	17.9	3.10	0.14
V09.CS07	1.28	13.14	4.11	0.22
V10.CS07	1.42	10.24	6.18	0.36
V11.CS07	1.57	8.32	6.77	0.38
V07.CS07	1.0	27.64	1.44	0.05
V07.CS08	0.87	21.74	2.14	0.09
V07.CS09	0.77	17.44	1.91	0.10
p.V10.CS07	1.42	11.58	5.35	0.29
p.V11.CS07	1.57	8.34	7.05	0.40
p.V18.CS07	2.57	4.02	30.5	0.69

We remark that the fluid temperature within $25 M$ from the black hole decreases more rapidly for high Mach numbers, so that the build up of the radiation pressure is faster for the highest Mach number. It should also be noted that while all perturbed models are radiation-pressure dominated in the upstream region after $t \sim 10\,000 M$, this regime is reached at different times by different models. Furthermore, even when radiation pressure dominates the dynamics, there could be isolated portions of the flow where the gas pressure is not completely negligible. This is the case, for instance, in the undulated downstream part of the flow, where the ratio of gas pressure to radiation pressures ratio can be as high as $p/\mathcal{P}_r \sim 0.1$.

The dominant role played by the radiation pressure is imprinted on the accretion rate for the p-model p.V18.CS07, as it is clear from Fig. 11. This model features the lowest quasi-equilibrium accretion rate and the highest luminosity. In general, we have found that the higher the Mach number, the higher the radiation pressure, and the

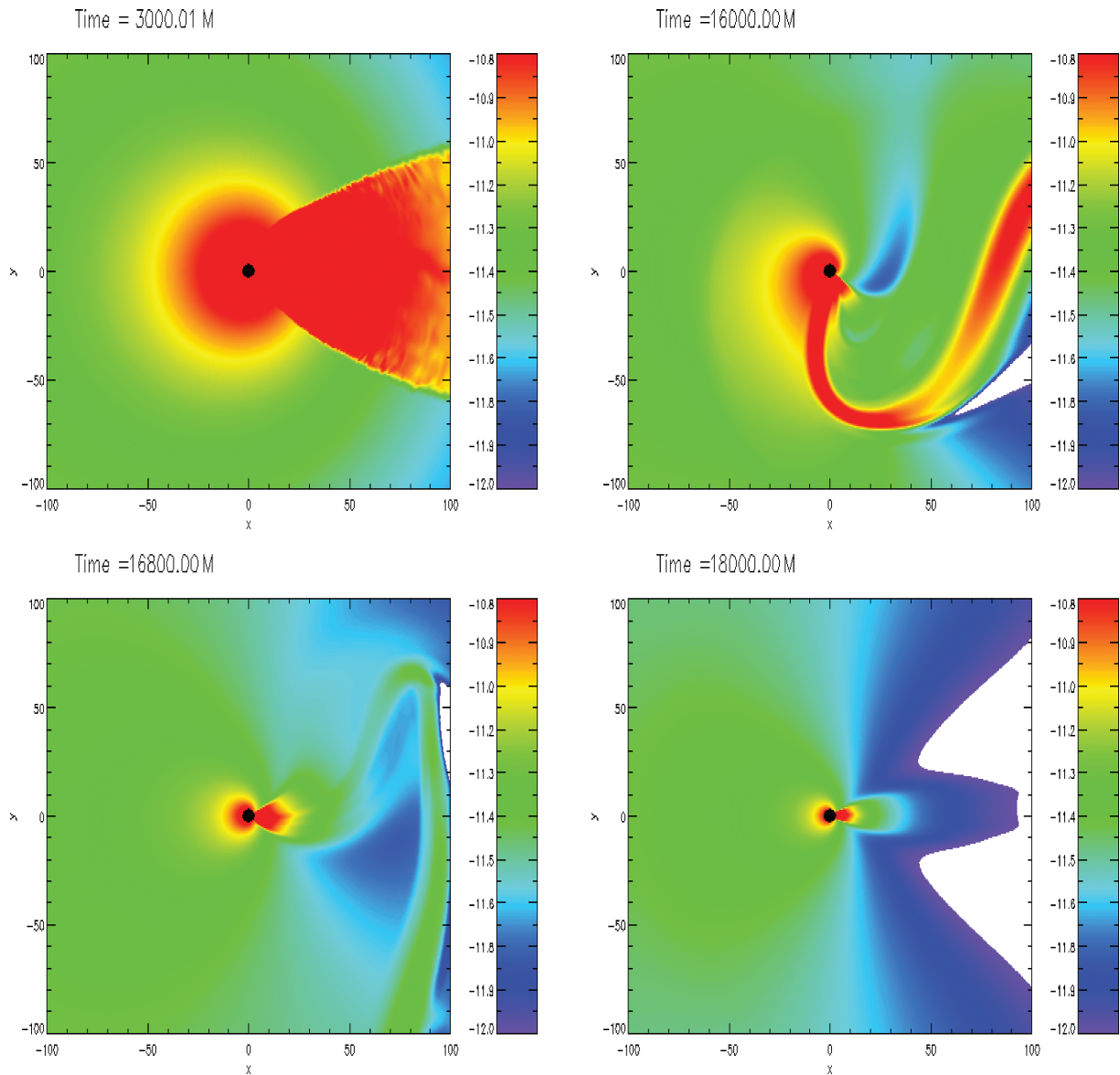


Figure 10. Rest-mass density in cgs units on a logarithmic scale for the perturbed Bondi–Hoyle model p.V10.CS07 at four different times in a radiation-hydrodynamic evolution. The two rows refer to different times of the evolution and white regions correspond to densities slightly below the threshold for the colour code at around 10^{-12} g/cm $^{-3}$. Note that a highly dynamical transient precedes the development of a stationary flow.

smaller the average density around the black hole. The perturbed model p.V18.CS07, for instance, has a rest-mass density which is a factor of 100 smaller than that in model p.V09.CS07, which has the minimum Mach number among the perturbed models and the longest relaxation time (cf. Fig. 11). At the same time, the accretion rate of p.V09.CS07 does not show the typical decline up until $t = 20000M$, although it is radiation-pressure dominated everywhere in the numerical domain. It is possible that the behaviour of model p.V09.CS07 would change, with the mass-accretion rate decreasing and the luminosity increasing, if the evolution was carried on a much longer time-scale.

4.3.3 Spinning black holes

Although the results presented so far refer to Schwarzschild black holes, a number of different simulations have been performed also for spinning black holes, with dimensionless spin parameters rang-

ing between 0 and 0.99. The interest, in these cases, was that of determining the influence that the black hole spin may have on the flow pattern and on the emission properties, for both the classical Bondi–Hoyle configurations and the perturbed ones.

Overall, the modifications introduced by the black hole spin are not particularly large to deserve a dedicated discussion. More specifically, as far as the dynamics is concerned, we have confirmed that as the spin of the black hole is increased, the shock cone that may form in the downstream part of the flow is progressively wrapped (this was originally pointed out by Font et al. 1999). This distortion, however, is evident only in the immediate vicinity of the horizon, and typically below $r \leq 20M$. Furthermore, very minor changes have been found in the light curves, to the point that the luminosity for an $a = 0.99$ black hole is only 3 per cent larger than that for an $a = 0$ Schwarzschild black hole. These results suggest that if spin-related signatures in the electromagnetic emission should exist and can be extracted, these will become evident only when a more

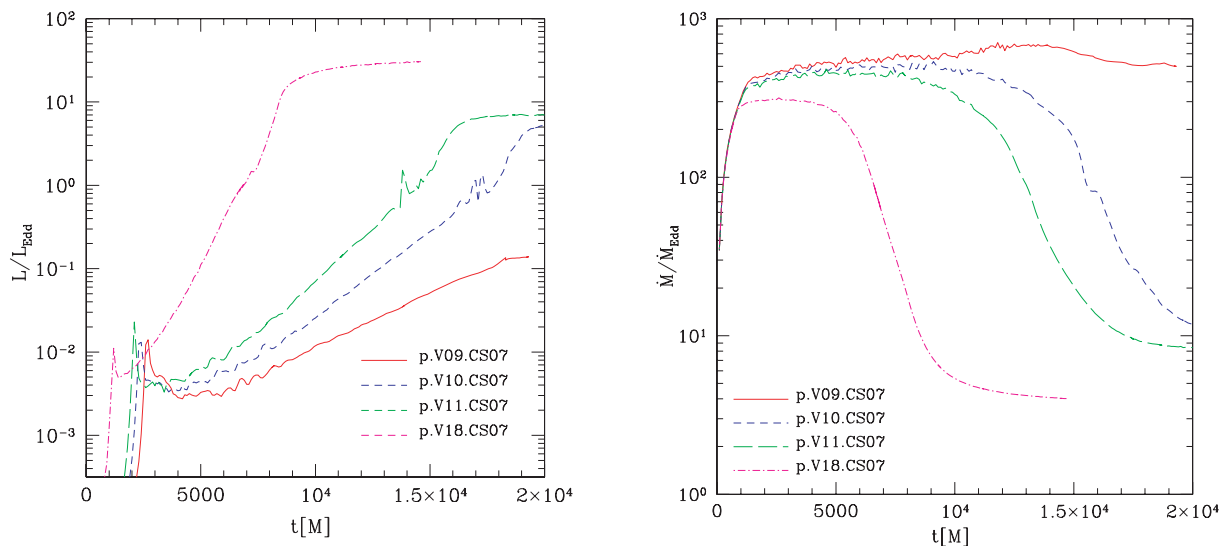


Figure 11. Left-hand panel: luminosity in Eddington units for the perturbed Bondi–Hoyle accretion flows. Right-hand panel: mass accretion rates in Eddington units for the same models in the left-hand panel.

sophisticated modelling of the emission processes (e.g. through inverse Compton in a rarefied corona) will be considered. This will be part of our future work.

4.3.4 Impact on electromagnetic counterparts of supermassive black hole binaries

Considerable attention has been recently dedicated to the possibility of detecting the electromagnetic counterpart of inspiral and merger of supermassive binary black holes (SMBBHs) systems. Such a detection would not only confirm the gravitational-wave detection and help us localize the source on the sky, but it would also provide a new tool for addressing a number of astrophysical questions (see e.g. Haiman et al. 2009). These include the possibility of testing models of galaxy mergers and clues on the mass distribution of supermassive black holes (see e.g. Sesana et al. (2011) and references therein).

Computing the EM counterpart to the inspiral of such a binary *is not* an aspect of our investigation and the physical conditions considered here badly match those expected in realistic scenarios describing this process, to which we plan to dedicate a separate investigation. The results obtained here, however, can shed some light on a common approximation made in numerical simulations aimed at estimating the luminosity from binary black hole mergers (Bode et al. 2010, 2011; Farris, Liu & Shapiro 2010, 2011; O’Neill et al. 2009; Megevand et al. 2009; Zanotti et al. 2010). All these works computed the bremsstrahlung luminosity without taking the back-reaction of the radiation into account, but rather performing a volume integral of the bremsstrahlung emissivity. The initial efforts to improve this treatment, but still without a proper radiation transfer, were initiated in Newtonian physics by Corrales, Haiman & MacFadyen (2010) by enforcing an isothermal evolution.

To prove our conjecture that the estimates made so far in terms of the bremsstrahlung luminosity are optimistic, providing cooling times that are too short, we have computed the bremsstrahlung luminosity emitted in the classical Bondi–Hoyle accretion of model V09.CS07 following the general-relativistic prescription adopted by the works cited above, namely

$$L_{\text{BR}} \simeq 3 \times 10^{78} \int (T^{1/2} \rho^2 \Gamma \sqrt{\gamma} dV) \left(\frac{M_{\odot}}{M} \right) \text{ erg s}^{-1}, \quad (43)$$

and compared the results obtained using the estimate (43) with those obtained through our radiative-transfer treatment. In addition, we have also considered an alternative calculation in which an isothermal evolution is enforced, and where it is assumed that all the changes in the temperature that are due to a local compression are dissipated as radiation. This idea, proposed in Newtonian framework by Corrales et al. (2010), has been extended to a general-relativistic context by Zanotti et al. (2010), and also used here for comparison.

The result of this comparison is shown in Fig. 12, where we have reported the three light curves computed according to the approaches described above. When stationarity is reached, i.e. at $t = 20\,000 M$, we find that $L_{\text{BR}}/L_{\text{Edd}} = 78$. This number should be contrasted with the result obtained through our self-consistent radiation-hydrodynamic simulations, which instead indicate $L/L_{\text{Edd}} = 4.11$

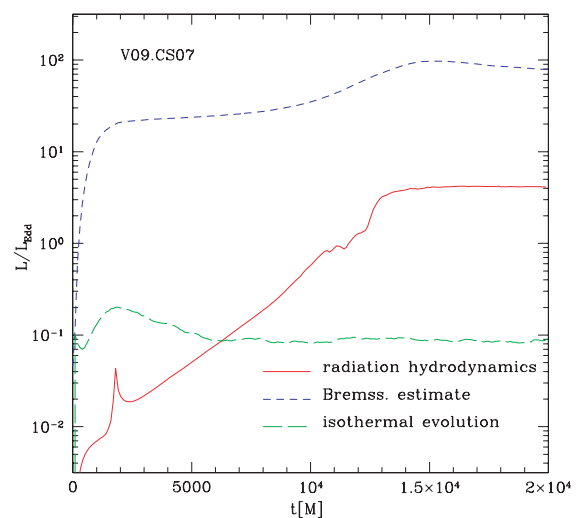


Figure 12. Comparison among light curves computed with different approaches. Solid red: luminosity obtained with the full radiation-hydrodynamic evolution according to equation (40). Dashed blue: luminosity obtained from equation (43). Long-dashed green: luminosity obtained through the isothermal evolution approximation (see text for more explanations).

(cf. Table 3). Interestingly, the luminosity obtained through the isothermal approximation provides a much smaller value, i.e. $L/L_{\text{Edd}} = 0.09$.

While this analysis is not exhaustive and has been performed in the specific scenario of an optically thick Bondi–Hoyle accretion, it does point out that the predictions made using the simplistic estimate of the bremsstrahlung luminosity via equation (43) provide light curves that are a factor of ~ 20 larger than those obtained with a more rigorous approach.

5 CONCLUSIONS

We have implemented and solved in an extension of the ECHO code (Del Zanna et al. 2007) the equations of relativistic radiation hydrodynamics in the optically thick regime and on a fixed black hole space–time when these equations are written in a conservation form (Farris et al. 2008). Within a $3 + 1$ split of space–time, we have discretized in time the set of equations with the method of lines and performed the evolution in time with a second-order modified Euler scheme. A fifth-order finite-difference algorithm based on an upwind monotonicity-preserving filter was employed for spatial reconstruction of primitive variables, whereas a two-wave HLL Riemann solver was used to ensure the shock-capturing properties. The new scheme has been successfully validated through a series of tests involving radiative shock tubes.

As a first application of the new code we have considered the emission properties of a hot Bondi–Hoyle accretion flow on to a black hole with the opacity given by Thomson scattering and thermal bremsstrahlung only. By considering different models with initial temperatures around $T \sim 10^{10}$ K, an ideal-gas EOS with adiabatic index $\gamma = 5/3$, and various sub-sonic and super-sonic regimes, we have found that the inclusion of radiation drastically alters the well-known dynamics of Bondi–Hoyle flows in all models considered. In particular, the system quickly enters a radiation-pressure-dominated regime, characterized by mass accretion rates that, once stationarity is reached, decrease by one or two orders of magnitude with respect to the purely hydrodynamical evolution. Nevertheless, the measured accretion rates are found to be always super-Eddington and as high as $\dot{M}/\dot{M}_{\text{Edd}} \sim 25$. This is in agreement with the expectation that the Eddington limit should hold strictly only in spherically symmetric flows. In addition, because the effective adiabatic index in the radiation-dominated pressure regime is smaller than the nominal one of the gas, the radiation can prevent the reversal of the shock cone that is typical of Bondi–Hoyle flows with low Mach numbers.

By computing the emitted luminosity through a surface integral over the radiative fluxes at the last optically thick surface, our approach has allowed the first self-consistent computation of the light curves for the Bondi–Hoyle flow, finding luminosities $L/L_{\text{Edd}} \simeq 1-7$. These results have been found to be independent of the initial conditions chosen for the intensity of the radiation energy density.

In addition to the classical Bondi–Hoyle accretion flows, we also performed simulations with perturbed setups, by injecting lower-temperature matter in the upstream region of the flow, which leads to highly dynamical transients reminiscent of the flip-flop instability (Foglizzo et al. 2005). Although the qualitative evolution of the accretion flow remains unchanged, the decreased initial temperature increases the time-scale over which the flow becomes radiation-pressure dominated and the accretion settles in a quasi-stationary state. In spite of these differences, we have found that the main features of the Bondi–Hoyle solution, such as the presence of the shock cone, persist under a wider class of physical conditions, even

in situations departing from stationarity. Overall, our results confirm and extend related Newtonian studies, such as those by Kley, Shankar & Burkert (1995).

Since we have shown that the luminosity is critically affected by the evolution of the *coupled* system of hydrodynamic and radiation equations, significant changes in the luminosities should be expected in those scenarios which have so far been modelled through a posteriori calculations to a purely hydrodynamical evolution. A first example in this respect is given by multi-colour black-body spectra, while a second example is represented by the calculation of electromagnetic counterpart to the inspiral of SMBBH systems (Bode et al. 2010, 2011; O’Neill et al. 2009; Zanotti et al. 2010; Farris et al. 2010, 2011). Postponing a more detailed calculation of this process to a future work, we have shown here that the calculation of the bremsstrahlung luminosities adopted in the above works leads to optimistic estimates, which should be regarded as upper limits.

ACKNOWLEDGMENTS

We are grateful to Luca Zampieri for many discussions and Alberto Sesana for important comments. We wish to thank Nico Budewitz for his help with the code and the AEI clusters. The computations were performed on the *datura* and *damiana* clusters at the AEI and on the IBM/SP6 of CINECA (Italy) through the ‘INAF-CINECA’ agreement 2008-2010. This work was supported in part by the DFG grant SFB/Transregio 7. Movies of the most relevant models are available at <http://www.olindozanotti.net/>

REFERENCES

- Arnowitz R., Deser S., Misner C. W., 1962, in Witten L., ed., *Gravitation: An Introduction to Current Research*. John Wiley, New York, p. 227
- Baiotti L., Hawke I., Montero P. J., Löffler F., Rezzolla L., Stergioulas N., Font J. A., Seidel E., 2005, *Phys. Rev. D*, 71, 024035
- Bode T., Haas R., Bogdanovic T., Laguna P., Shoemaker D., 2010, *ApJ*, 715, 1117
- Bode T., Bogdanovic T., Haas R., Healy J., Laguna P., Shoemaker D., 2011, preprint (arXiv:1101.4684)
- Bruenn S. W., Nisco K. R. D., Mezzacappa A., 2001, *ApJ*, 560, 326
- Corrales L. R., Haiman Z., MacFadyen A., 2010, *MNRAS*, 404, 947
- Del Zanna L., Zanotti O., Bucciantini N., Londrillo P., 2007, *A&A*, 473, 11
- Dönmez O., Zanotti O., Rezzolla L., 2010, *MNRAS*, 412, 1659
- Duez M. D., 2010, *Class. Quantum Grav.*, 27, 114002
- Edgar R., 2004, *New Astron. Rev.*, 48, 843
- Farris B. D., Li T. K., Liu Y. T., Shapiro S. L., 2008, *Phys. Rev. D*, 78, 024023
- Farris B. D., Liu Y. T., Shapiro S. L., 2010, *Phys. Rev. D*, 81, 084008
- Farris B. D., Liu Y. T., Shapiro S. L., 2011, *Phys. Rev. D*, 84, 024024
- Foglizzo T., Galletti P., Ruffert M., 2005, *A&A*, 435, 397
- Font J. A., Ibáñez J. M., 1998, *ApJ*, 494, 297
- Font J. A., Ibáñez J. M., Papadopoulos P., 1998, *ApJ*, 507, L67
- Font J. A., Ibáñez J. M., Papadopoulos P., 1999, *MNRAS*, 305, 920
- Gilden D. L., Wheeler J. C., 1980, *ApJ*, 239, 705
- Gnedin N. Y., Abel T., 2001, *New Astron.*, 6, 437
- Guess A. W., 1960, *Phys. Fluids*, 3, 697
- Haiman Z., Kocsis B., Menou K., Lippai Z., Frei Z., 2009, *Class. Quantum Grav.*, 26, 094032
- Harwit M., 1998, *Astrophysical Concepts*. Springer, New York
- Herant M., Benz W., Hix W. R., Fryer C. L., Colgate S. A., 1994, *ApJ*, 435, 339
- Hsieh S., Spiegel E. A., 1976, *ApJ*, 207, 244
- Janka H.-T., Mueller E., 1995, *ApJ*, 448, L109
- Janka H.-T., Mueller E., 1996, *A&A*, 306, 167
- Kley W., Shankar A., Burkert A., 1995, *A&A*, 297, 739

Liebendörfer M., Mezzacappa A., Thielemann F.-K., Messer O. E. B., Hix W. R., Bruenn S. W., 2001, *Phys. Rev. D*, 63, 103004

Liebendörfer M., Rampp M., Janka H., Mezzacappa A., 2005, *ApJ*, 620, 840

McWilliams S. T., 2011, *Class. Quantum Grav.*, 28, 134001

Megevand M., Anderson M., Frank J., Hirschmann E. W., Lehner L., Liebling S. L., Motl P. M., Neilsen D., 2009, *Phys. Rev. D*, 80, 024012

Messer O. E. B., Bruenn S. W., Blondin J. M., Hix W. R., Mezzacappa A., 2008, *J. Phys. Conf. Ser.*, 125, 012010

Mezzacappa A., Liebendörfer M., Messer O. E. B., Hix W. R., Thielemann F.-K., Bruenn S. W., 2001, *Phys. Rev. Lett.*, 86, 1935

Mihalas D., Mihalas B., 1999, *Foundations of Radiation Hydrodynamics*. Dover, New York

Mösta P., Palenzuela C., Rezzolla L., Lehner L., Yoshida S., Pollney D., 2010, *Phys. Rev. D*, 81, 064017

Müller B., Janka H.-T., Dimmelmeier H., 2010, *ApJS*, 189, 104

Noble S. C., Krolik J. H., Hawley J. F., 2009, *ApJ*, 692, 411

Novikov I. D., Thorne K. S., 1973, in De Witt C., De Witt B. S., eds, *Black Holes (Les Astres Occlus)*. Gordon and Breach, New York, p. 343

O'Neill S. M., Miller M. C., Bogdanović T., Reynolds C. S., Schnittman J. D., 2009, *ApJ*, 700, 859

Palenzuela C., Anderson M., Lehner L., Liebling S. L., Neilsen D., 2009, *Phys. Rev. Lett.*, 103, 081101

Park M., 2006, *MNRAS*, 367, 1739

Penner A. J., 2011, *MNRAS*, 414, 1467

Petkova M., Springel V., 2009, *MNRAS*, 396, 1383

Petkova M., Springel V., 2010, preprint (arXiv e-prints)

Petrich L. I., Shapiro S. L., Stark R. F., Teukolsky S. A., 1989, *ApJ*, 336, 313

Rezzolla L., Miller J. C., 1994, *Class. Quantum Grav.*, 11, 1815

Rezzolla L., Giacomazzo B., Baiotti L., Granot J., Kouveliotou C., Aloy M. A., 2011, *ApJ*, 732, L6

Ruffert M., 1996, *A&A*, 311, 817

Rybicki G. B., Lightman A. P., 1986, *Radiative Processes in Astrophysics*. Wiley-VCH, New York

Schwartz R. A., 1967, *Ann. Phys.*, 43, 42

Sekiguchi Y., 2010, *Progress Theor. Phys.*, 124, 331

Sekiguchi Y., Kiuchi K., Kyutoku K., Shibata M., 2011, *Phys. Rev. Lett.*, 107, D51102

Sesana A., Gair J., Berti E., Volonteri M., 2011, *Phys. Rev. D*, 83, 044036

Shapiro S. L., 1996, *ApJ*, 472, 308

Shibata M., Kiuchi K., Sekiguchi Y., Suwa Y., 2011, *Theoretical Phys.*, 125, 1255

Smarr L., York J. W., 1978, *Phys. Rev. D*, 17, 2529

Szöke A., Brooks E. D., III, McKinley M. S., Daffin F. C., 2006, in Graziani F., ed., *Computational Methods in Transport Accurate and Efficient Radiation Transport in Optically Thick Media by Means of the Symbolic Implicit Monte Carlo Method in the Difference Formulation*. Springer, Berlin, p. 255

Takahashi R., 2007, *MNRAS*, 382, 1041

Thorne K. S., 1981, *MNRAS*, 194, 439

Vitello P., 1984, *ApJ*, 284, 394

Zampieri L., Miller J. C., Turolla R., 1996, *MNRAS*, 281, 1183

Zanotti O., Rezzolla L., Del Zanna L., Palenzuela C., 2010, *A&A*, 523, A8

APPENDIX A: EXTENDED GEOMETRIZED SYSTEM OF UNITS

We recall that the definition of geometric units of time and lengths is obtained by setting the speed of light c and the gravitational constant G to pure numbers. This implies that seconds and grams of the cgs system can be written as

$$1 \text{ s} = 2.997924 \times 10^{10} \left(\frac{1}{c} \right) \text{ cm} \quad (\text{A1})$$

$$1 \text{ g} = 7.424157 \times 10^{-29} \left(\frac{c^2}{G} \right) \text{ cm}. \quad (\text{A2})$$

Within this general setup, a convenient unit of space is still required. The cm is of course a bad choice and the gravitational radius $r_g = GM/c^2$ is instead chosen. In order for this new unit to be convenient with respect to the centimetre, the mass M of the system has to be sufficiently large. From the physical value of the solar mass and from (A2) we find the relation between the cgs units and the new unit of length r_g

$$1 \text{ cm} = 6.772289 \times 10^{-6} \left(\frac{M_\odot}{M} \right) r_g, \quad (\text{A3})$$

$$1 \text{ s} = 2.030281 \times 10^5 \left(\frac{1}{c} \right) \left(\frac{M_\odot}{M} \right) r_g, \quad (\text{A4})$$

$$1 \text{ g} = 5.027854 \times 10^{-34} \left(\frac{c^2}{G} \right) \left(\frac{M_\odot}{M} \right) r_g. \quad (\text{A5})$$

It is also useful to explicitly write the conversion of rest-mass density and luminosity between the two systems, namely

$$\rho_{\text{cgs}} = 6.1776 \times 10^{17} \left(\frac{G}{c^2} \right) \left(\frac{M_\odot}{M} \right)^2 \rho_{\text{geo}}, \quad (\text{A6})$$

$$L_{\text{cgs}} = 3.6292 \times 10^{59} \left(\frac{G}{c^5} \right) L_{\text{geo}}, \quad (\text{A7})$$

where ρ_{cgs} and ρ_{geo} (as well as L_{cgs} and L_{geo}) are the pure numbers expressing the mass density (as well as the luminosity) in the cgs system and in the geometrized system, respectively. In the traditional geometrized system c and G are set equal to unity. However, for specific physical applications where very low mass densities are encountered, the corresponding value of ρ_{geo} may become prohibitively small. For this reason, it is convenient to assume a smaller value of G , such as $G = 10^{-10}$.

For convenience, we report the Eddington luminosity and the Thomson scattering opacity of electrons in geometrized units, namely

$$L_{\text{Edd}} = 3.4636 \times 10^{-22} \left(\frac{c^5}{G} \right) \left(\frac{M}{M_\odot} \right), \quad (\text{A8})$$

$$\chi_e^s = 3.628 \times 10^{22} G \rho_{\text{geo}} \left(\frac{M_\odot}{M} \right). \quad (\text{A9})$$

The extension of the geometrized system of units to the temperature can be obtained by setting to a pure number any physical constant containing the temperature. In this paper we have chosen to set $m_p/k_B = 1$, where m_p is the mass of the proton, while k_B is the Boltzmann constant. In this way the temperature is a dimensionless quantity and the transformation of the temperature from the dimensionless values to Kelvin is given by

$$T_K = 1.088 \times 10^{13} T_{\text{geo}}. \quad (\text{A10})$$

In these *extended* geometrized units the radiation constant $a_{\text{rad}} = 4\sigma/c$ becomes

$$a_{\text{rad}} = 0.191495 \left(\frac{1}{G} \right) \left(\frac{M}{M_\odot} \right)^2 r_g^{-2}. \quad (\text{A11})$$

This paper has been typeset from a $\text{\TeX}/\text{\LaTeX}$ file prepared by the author.